


A novel black hole mass scaling relation based on coronal gas, and its dependence with the accretion disc

Almudena Prieto¹  ¹★, Alberto Rodríguez-Ardila,^{2,3} Swayamtrupta Panda^{4,5} and Murilo Marinello²

¹*Instituto de Astrofísica de Canarias & Universidad de La Laguna, E-38205 Tenerife, Spain*

²*LNA/MCTIC, Rua dos Estados Unidos, 154. Bairro das Nações, Itajubá, MG B-37501-591, Brazil*

³*Divisão de Astrofísica, INPE, Avenida dos Astronautas 1758, São José dos Campos, B-12227-010 SP, Brazil*

⁴*Center for Theoretical Physics, Polish Academy of Sciences, Al. Lotników 32/46, PL-02-668 Warsaw, Poland*

⁵*Nicolaus Copernicus Astronomical Center, Polish Academy of Sciences, ul. Bartycka 18, PL-00-716 Warsaw, Poland*

Accepted 2021 November 11. Received 2021 October 12; in original form 2021 June 24

ABSTRACT

Using *bona-fide* black hole (BH) mass estimates from reverberation mapping and the line ratio $[\text{Si VI}] 1.963\mu\text{m}/\text{Br}\gamma_{\text{broad}}$ as tracer of the AGN ionizing continuum, a novel BH-mass scaling relation of the form $\log(M_{\text{BH}}) = (6.40 \pm 0.17) - (1.99 \pm 0.37) \times \log([\text{Si VI}]/\text{Br}\gamma_{\text{broad}})$, dispersion 0.47 dex, over the BH mass interval, 10^6 – $10^8 M_{\odot}$ is found. Following on the geometrically thin accretion disc approximation and after surveying a basic parameter space for coronal lines production, we believe one of main drivers of the relation is the effective temperature of the disc, which is effectively sampled by the $[\text{Si VI}] 1.963\mu\text{m}$ coronal line for the range of BH masses considered. By means of CLOUDY photoionization models, the observed anticorrelation appears to be formally in line with the thin disc prediction $T_{\text{disc}} \propto M_{\text{BH}}^{-1/4}$.

Key words: accretion, accretion discs – radiation mechanism thermal – techniques: spectroscopic – galaxies: active – quasars: emission lines.

1 INTRODUCTION

The determination of black hole (BH) masses is a major focus in the community. Most accurate determinations rely on dynamical analysis, for galaxies including our Milky Way. That approach, though, gets restricted to relative nearby objects, where high angular observations resolving the BH radius of influence or extensive variability monitoring programs of the broad-line region in active galactic nuclei (AGN) are possible (e.g. Peterson 1993; Genzel, Eisenhauer & Gillessen 2010; Kormendy & Ho 2013; Bentz & Katz 2015). Most BH mass estimates are based, however, on powerful correlations between the BH mass and the bulge stellar velocity dispersion – the M – σ relation (e.g. Ferrarese & Merritt 2000; Gültekin et al. 2009), or the AGN continuum luminosity – so-called mass–luminosity relation by which the optical, UV, or X-ray luminosity are found to correlate with the Broad-Line-Region (BLR) size (e.g. Koratkar & Gaskell 1991; Kaspi et al. 2000, 2005; Landt et al. 2013, and references therein).

While the use of the M – σ relation requires the measurement of σ , it is not always easy to determine it, particularly in AGN. In these objects, the strong continuum from the nuclear region dilutes the stellar absorption lines. In order to overcome this difficulty, a number of alternative scaling relations using emission lines such as $[\text{O III}] \lambda 5007$ to measure the mass of the bulge (e.g. Nelson & Whittle 1996), $[\text{O II}] \lambda 3727$ (e.g. Salviander et al. 2006), $\text{H}\beta$ or $\text{H}\alpha$ (e.g. Kaspi et al. 2005; Greene & Ho 2005) to infer on the BLR size,

or $[\text{Fe II}]$ in the near-infrared (e.g. Riffel et al. 2013) to infer on the stellar σ , have been proposed.

Overall, the scatter of the scaling relations in the literature is 40 per cent or larger. A fraction of the scatter should be intrinsic, inherent to the nature of the parameters used in the relations and their variations between objects. The Hubble type and chiefly, the presence of bulges or pseudo-bulges affect the M – σ relation (Gültekin et al. 2009). An intrinsic scatter of up 40 per cent in the continuum luminosity – BLR size scaling relation is inferred by Kaspi et al. (2005), mostly introduced by changes in the optical – UV continuum shape with increasing AGN luminosity. Other factors such as intrinsic differences in the BLR density and the ionization parameter are also expected to play a role (Collin-Souffrin et al. 1988; Marziani et al. 2019; Panda 2021).

With the start of operations of facilities optimized for the near – mid-Infrared (IR) region, the James-Webb Space Telescope (e.g. Gardner et al. 2006) and the Vera Rubin Observatory’s LSST (e.g. Ivezić et al. 2019), the use of scaling-relations focused on spectral features centred in that interval will be an asset. This paper presents a novel approach to estimate BH masses as a function of high ionization IR emission lines, namely the coronal lines, after normalization to HI broad-line emission, so far for Type I AGN only. The motivation behind relies on the high ionization potential, IP, of coronal lines, above 50 eV up to few hundreds eV which makes them excellent tracers of the ionizing continuum. Hence, their ability to sample the peak – or highest temperature, of the ionizing continuum whether this is dominated by a thermal component, an accretion disc or blackbody modified spectrum.

Coronal lines (CL) spread over the X-rays, optical and IR spectrum. Although often fainter than the classical medium-ionization

* E-mail: aprieto@iac.es

lines used for photoionization diagnosis, high angular resolution in nearby AGN has shown that CL particularly in the near-IR are among the most conspicuous features (e.g. Marconi et al. 1994; Reunanen, Kotilainen & Prieto 2003; Prieto, Marco & Gallimore 2005; Rodríguez-Ardila et al. 2006, 2017; Müller-Sánchez et al. 2011; Gravity Collaboration 2020).

In this work, we explore possible dependencies of the BH mass with optical and infrared coronal emission of different IP after normalizing of the coronal emission to the nearest H I broad-line emission. The CLs employed are the most common and brightest ones in AGN (Reunanen et al. 2003; Rodríguez-Ardila et al. 2011; Lamperti et al. 2017). A tight correlation between BH mass and the CL ratio $[\text{Si VI}] 1.96 \mu\text{m} / Br_{\text{gamma}}$ is observed. Possible explanations for the observed correlation (and the absence of it for some other CLs) are examined in the context of accretion theory and photoionization model predictions.

The paper is organized as follows. Section 2 describes the observations and data reduction employed in this work; Section 3 deals with the diagnostics diagrams developed by us to weigh the BH mass using CL; Section 4 examines the scaling relationship in the framework of accretion theory and photoionization predictions. The implications and limitations of the results are presented in Section 5. Throughout this paper, the following cosmology is adopted: $H_0 = 70 \text{ km s}^{-1} \text{ Mpc}^{-1}$, $\Omega_M = 0.30$, $\Omega_\Lambda = 0.70$.

2 DATA SELECTION

Objects in this work are selected by having BH masses determined by reverberation mapping and single epoch optical and/or near-IR spectra with accurate CL measurements. The first criterion restricts the sample to Type I sources only. The second avoids variability issues. Although we give preference to sources with both optical and near-IR spectra available, this final criterion could not always be fulfilled.

The CL used are $[\text{Fe VII}] \lambda 6087 \text{ \AA}$ in the optical and $[\text{S VIII}] 0.991 \mu\text{m}$, $[\text{Si X}] 1.432 \mu\text{m}$, and $[\text{Si VI}] 1.964 \mu\text{m}$ in the near-IR. They are among the strongest CL in AGN (Reunanen et al. 2003; Rodríguez-Ardila et al. 2011; Lamperti et al. 2017) and span a wide IP range, 100–350 eV. In addition, H II lines of $\text{H}\beta$, $\text{Pa}\beta$, and $\text{Br}\gamma$ are employed. The whole set samples the ionizing continuum over the 13.6–351 eV range. Near-IR CL were preferred because of their reduced extinction. Optical CL $[\text{Fe VII}]$ was also selected because of its strength, still moderate extinction, and IP close to that of $[\text{Si VI}]$.

The final working sample of objects has 31 AGN (Table 1). It includes BH masses, most from Bentz & Katz (2015) compilation, coronal line ratios measured from spectra in this work or from spectra already described in other publications, and data sources. For a subsample, optical and near-IR data are presented in this work for the first time. Table 2 lists these later sources with details of the observations, including telescope or instrument employed, date of observation, airmass, and exposure time.

2.1 Optical spectroscopy

Optical spectra were taken from a variety of sources, as indicated in the last column of Table 1. In more than half of the sample, spectra from the Sloan Digital Sky Survey (SDSS) data release 7 (Abazajian et al. 2009) were employed. SDSS delivers fully wavelength and flux calibrated spectra. Therefore, data reduction for these objects will not be discussed here. Similarly, archival flux-calibrated spectra

for Ark 564 taken by the Faint Object Spectrograph (FOS) on-board the *Hubble Space Telescope* (HST) were employed. Details of observations and reduction of this target will not be addressed here. NGC 4051 employs archival spectroscopy available from the NASA’s Extragalactic Database (NED). Details of that observation can be found in Moustakas & Kennicutt (2006). Mrk 335 was observed using the 2.15 m telescope at the Complejo Astronómico El Leoncito (CASLEO). Details of the observations and data reduction are in Rodríguez-Ardila et al. (2002). Fully reduced spectra for Fairall 9, NGC 4151, and Mrk 509 were extracted from the AGN Watch Project.¹

The second major source of optical data is the 4.1 m Southern Observatory for Astrophysical Research (SOAR) Telescope at Cerro Pachon, Chile. The observations were carried out using the Goodman Spectrograph (Clemens, Crain & Anderson 2004), equipped with a 600 l/mm grating and a 0.8 arcsec slit width, giving a resolution $R \sim 1500$. In addition to the science frames, standard stars (Baldwin & Stone 1984) were observed for flux calibration. The average seeing of the observations was ~ 1 arcsec. None of the nights were photometric, implying that the flux calibration is relative. Accordingly, no attempt was made to put the optical and NIR data on the same flux scale. Hg-Ar arc lamps were taken after the science frames for wavelength calibration. Daytime calibrations include bias and flat-field images.

The data were reduced using standard IRAF tasks. It includes subtraction of the bias level and division of the science and flux standard star frames by a normalized master flat-field image. Thereafter, the spectra were wavelength calibrated by applying the dispersion solution obtained from the arc lamp frames. Finally, the spectra of standard stars were extracted and combined to derive the sensitivity function, later applied to the 1D science spectra. The final products are wavelength and flux calibrated optical spectra.

In all cases above, the final spectra were corrected for Galactic extinction using the extinction maps of Schlafly & Finkbeiner (2011) and the Cardelli, Clayton & Mathis (1989) extinction law. Figs A1–A4 show the optical spectra employed in this work.

2.2 NIR spectroscopy

Most of the NIR emission line flux ratios employed in this work were extracted from Riffel, Rodríguez-Ardila & Pastoriza (2006). For targets not reported in that publication, observations were obtained using either the Gemini Near-Infrared Spectrograph (GNIRS) attached to the Gemini North Telescope or the ARCOiRIS spectrograph, mounted on either Blanco or SOAR Telescopes. Note that ARCOiRIS was installed on Blanco since 2017 and up to 2019, when it was then moved to SOAR with no modifications regarding their setup. Below we describe the observations and data reduction procedures, noting that no distinction between Blanco and SOAR is made. Both data collection and treatment is made employing the same observing strategy and reduction pipelines.

Figs A5–A7 show the final reduced NIR spectra for those galaxies not reported in Riffel et al. (2006).

2.2.1 ARCOiRIS Blanco or SOAR data

NIR spectra of Fairall 9, 3C 120, Mrk 707, NGC 3783, Mrk 1310, Mrk 841, and NGC 6814 were obtained using the ARCOiRIS spectrograph attached to either the 4 m Blanco Telescope or the 4.1 m SOAR telescope. The science detector employed is a 2048×2048

¹<http://www.astronomy.ohio-state.edu/agnwatch/>

Table 1. Black hole mass and Coronal Line ratios for the galaxies sample.

Galaxy	$\log M_{\text{BH}}^1$	[Fe VII]/H β^2	[Si VI]/Br γ^3	[Si X]/Pa β	[S VIII]/Pa β
Mrk 335	7.23 \pm 0.04	0.077 \pm 0.009	0.40 \pm 0.09 ^e	0.04 \pm 0.01	0.022 \pm 0.006
Fairall 9	8.29 \pm 0.09	0.038 \pm 0.003	0.11 \pm 0.02 ^f	0.08 \pm 0.01	0.04 \pm 0.01
NGC 863	7.57 \pm 0.06	...	0.24 \pm 0.07 ^e
3C 120	7.74 \pm 0.04	...	0.33 \pm 0.06 ^f	0.08 \pm 0.02	0.03 \pm 0.01
Mrk 707	6.50 \pm 0.10 ^a	0.025 \pm 0.002	0.38 \pm 0.04 ^f
Mrk 110	7.29 \pm 0.10	0.05 \pm 0.002
NGC 3227	6.78 \pm 0.10	...	0.75 \pm 0.20	...	0.012 \pm 0.004
Mrk 142	6.29 \pm 0.10	0.02 \pm 0.004
SBS 1116+583A	6.56 \pm 0.09	0.01 \pm 0.002
PG 1126–041	8.08 \pm 0.03 ^b	...	0.28 \pm 0.02	0.04 \pm 0.01	0.025 \pm 0.002
NGC 3783	7.37 \pm 0.08	0.052 \pm 0.002	0.42 \pm 0.09 ^f	0.05 \pm 0.01	0.023 \pm 0.003
Mrk 1310	6.21 \pm 0.08	0.032 \pm 0.002	0.57 \pm 0.17 ^f	0.06 \pm 0.01	0.06 \pm 0.01
NGC 4051	6.13 \pm 0.12	0.123 \pm 0.012	0.96 \pm 0.11	0.33 \pm 0.02	0.205 \pm 0.030
NGC 4151	7.55 \pm 0.05	0.02 \pm 0.001	0.51 \pm 0.05	0.05 \pm 0.01	0.057 \pm 0.003
Mrk 202	6.13 \pm 0.17	0.033 \pm 0.004
Mrk 766	6.82 \pm 0.05	0.03 \pm 0.002 ^d	0.78 \pm 0.10	0.05 \pm 0.01	0.045 \pm 0.002
Mrk 50	7.42 \pm 0.06	0.005 \pm 0.001
NGC 4395	5.45 \pm 0.13	0.092 \pm 0.005	1.18 \pm 0.10 ^f	0.02 \pm 0.01	0.053 \pm 0.006
Mrk 771	7.76 \pm 0.20	0.03 \pm 0.002
NGC 4748	6.41 \pm 0.11	...	0.93 \pm 0.06	0.06 \pm 0.02	0.137 \pm 0.042
PG 1307+085	8.54 \pm 0.13	0.01 \pm 0.002
MGC-6-30–15	6.60 \pm 0.12	0.017 \pm 0.002
NGC 5548	7.72 \pm 0.02	0.044 \pm 0.003	0.61 \pm 0.09	0.11 \pm 0.01	0.122 \pm 0.011
PG 1448+273	6.97 \pm 0.08	...	0.57 \pm 0.11
Mrk 290	7.28 \pm 0.02	0.023 \pm 0.002
Mrk 841	8.10 \pm 0.02 ^c	0.008 \pm 0.002	0.20 \pm 0.06 ^f	0.02 \pm 0.01	0.024 \pm 0.002
3C 390.3	8.64 \pm 0.04	0.018 \pm 0.001
NGC 6814	7.04 \pm 0.06	...	0.13 \pm 0.02 ^f
Mrk 509	8.05 \pm 0.04	...	0.17 \pm 0.02
Ark 564	6.59 \pm 0.17	0.056 \pm 0.007	1.08 \pm 0.10	0.30 \pm 0.01	0.101 \pm 0.006
NGC 7469	6.96 \pm 0.05	0.021 \pm 0.001	0.60 \pm 0.05	0.07 \pm 0.01	0.037 \pm 0.006

Notes. All the line ratios are normalized to the broad component of H I. Individual line fluxes are listed in Table A1 1. Masses are from Bentz & Katz (2015) unless stated otherwise; (a) – Park et al. (2017); (b) – Dasyra et al. (2007); (c) – Woo & Urry (2002). 2. [Fe VII] ratio is determined in this work unless stated otherwise: (d) – Rodríguez-Ardila, Contini & Viegas (2005). 3. The NIR emission-line flux ratios are from Riffel et al. (2006) except when indicated: (e) – Rodríguez-Ardila et al. (2002); (f) – This work.

Table 2. Sub-sample of galaxies with observations first presented in this work.

Galaxy	RA hh.mm.ss	DEC deg.mm.ss	Redshift (z)	Telescope/ Instrument	Date of Observation	A_λ V mag	Airmass	$N_{\text{exp}} \times T_{\text{exp}}$ (sec)
Fairall 9	01:23:45.8	−58:48:21	0.04614	SOAR/TSpec4	2019 Aug 08	0.071	1.22	20x180
3C 120	04:33:11.1	05:21:16	0.03301	SOAR/TSpec4	2020 Feb 10	0.816	1.28	12x180
Mrk 707	09:37:01.03	01:05:43.48	0.05025	Blanco/ARCOiRIS	2017 Apr 09	0.189	1.21	28x180
				SOAR/Goodman	2017 Mar 11		1.18	3x900
NGC 3783	11:39:01.7	−37:44:19	0.00973	Blanco/ARCOiRIS	2017 Apr 10	0.332	1.05	16x180
				SOAR/Goodman	2011 Jan 31		1.10	3x900
Mrk 1310	12:01:14.3	−03:40:41	0.01956	Blanco/ARCOiRIS	2017 Apr 08	0.083	1.18	20x180
				SOAR/Goodman	2012 May 21		1.24	3x1800
MGC-6-30–15	13:35:53.7	−34:17:44	0.00749	SOAR/Goodman	2011 Apr 01	0.165	1.05	3x1200
Mrk 841	15:04:01.2	10:26:16.15	0.03642	Blanco/ARCOiRIS	2017 Apr 08	0.082	1.42	12x180
				SOAR/Goodman	2017 Mar 11		1.36	2x900
NGC 6814	19:42:40.6	−10:19:25	0.00521	Blanco/ARCOiRIS	2017 Apr 10	0.509	1.38	20x180
NGC 7469	23:03:15.6	+ 08:52:26	0.01632	SOAR/Goodman	2010 Nov 11	0.188	1.34	3x900

Hawaii-2RG Hg-Cd-Te array with a sampling of $0.41 \text{ arcsec pixel}^{-1}$. The slit assembly is 1.1 arcsec wide and 28 arcsec long. The delivered spectral resolution R is ~ 3500 across the different dispersion orders. Observations were done nodding in two positions along the slit. Right before or after the science target, a telluric star, close in airmass to the former, was observed to remove telluric features and to perform the flux calibration. Cu-Hg-Ar frames were also observed at the same position as the galaxies for wavelength calibration.

The spectral reduction, extraction, and wavelength calibration procedures were performed using SPEXTOOL V4.1, an IDL-based software developed and provided by the SpeX team (Cushing, Vacca & Rayner 2004) with some modifications specifically designed for the data format and characteristics of ARCoIRIS, written by Dr. Katelyn Allers (private communication). Telluric features removal and flux calibration were done using XTELLCOR (Vacca, Cushing & Rayner 2003). The different orders were merged into a single 1D spectrum from 1 to $2.4 \text{ }\mu\text{m}$ using the XMERGEORDERS routine. We then corrected these data for Galactic extinction using the Cardelli et al. (1989) law and the extinction maps of Schlafly & Finkbeiner (2011).

2.2.2 GNIRS or Gemini spectroscopy

Near-infrared spectra of NGC 4395 and Ark 564 were collected using GNIRS (Elias et al. 2006) in the cross-dispersed mode. It allows simultaneous z , J , H , and K -band observations, covering the spectral range $0.8\text{--}2.5 \text{ }\mu\text{m}$ in a single exposure. GNIRS science detector consist of an ALADDIN $1\text{k} \times 1\text{k}$ In-Sb array. The instrument setup includes a 32 l/mm grating and a $0.8 \times 7 \text{ arcsec}$ slit, giving a spectral resolution of $R \sim 1300$ (or 320 km s^{-1} FWHM). Individual exposures were taken, nodding the source in a ABBA pattern along the slit. Right after the observation of the science frames, an A0V star was observed at a similar airmass, with the purpose of flux calibration and telluric correction.

The NIR data were reduced using the XDBGNIRS pipeline (v2.0),² which delivers a fully reduced, wavelength and flux calibrated, 1D spectrum with all orders combined (Mason et al. 2015). Briefly, the pipeline cleans the 2D images from radiative events and prepares a master flat constructed from quartz IR lamps to remove pixel to pixel variation. Thereafter, the s -distortion solution is obtained from daytime pinholes flats and applied to the science and telluric images to rectify them. Argon lamp images are then used to find the wavelength dispersion solution, followed by the extraction of 1D spectra from the combined individual exposures. The telluric features from the science spectrum are removed using the spectrum of an A0V star. Finally, the flux calibration is achieved assuming a blackbody shape for the standard star (Pecaut & Mamajek 2013) scaled to its K -band magnitude (Skrutskie et al. 2006). The different orders are combined in to a single 1D spectrum and corrected for Galactic extinction using the Cardelli et al. (1989) law and the extinction maps of Schlafly & Finkbeiner (2011). The spectra of these two sources are not presented here as they are shown in Mason et al. (2015).

In order to measure the flux of the lines for the sub-sample of objects described above, we modelled the observed profiles with a suitable function that best represents them and then integrated the flux under that function. This was done via a least-square fit of a model line profile (Gaussian, Lorentzian, or Voigt functions) to a given line or set of blended lines to determine the flux, peak position, and FWHM of the individual components. Typically, one or two Gaussian components were necessary to represent the coronal

lines. For the permitted lines of H I a broad component associated to the BLR was employed. In this process, the underlying continuum emission was approximated by a linear fit.

For the optical part, the measurement of the $H\beta$ flux was preceded by the removal of the underlying power-law continuum and the pseudo-continuum produced by the Fe II lines that contaminates $H\beta$. This was done following the prescription of Boroson & Green (1992).

Table 1 shows the measured optical emission-line flux ratio between [Fe VII] $\lambda 6087$ and the broad component of $H\beta$ (column 3) and the NIR ratios for [Si VI] $1.964 \text{ }\mu\text{m}/\text{Br}\gamma$ (column 4), [Si X] $1.431 \text{ }\mu\text{m}/\text{Pa}\beta$ (column 5), and [S VIII] $0.9914 \text{ }\mu\text{m}/\text{Pa}\beta$ (column 6). For the later three ratios the flux associated to the broad component of the Brackett or Paschen lines was employed. Table A1 in the Appendix lists the individual fluxes of all lines employed in this work. Note that because the optical and NIR spectra were taken on different dates and in most cases, different telescopes, the intrinsic line ratios $H\beta/\text{Pa}\beta$ and $H\beta/\text{Br}\gamma$ may depart from their theoretical value. This, however, does not affect our results as we do not use line ratios that combine both spectral regions. However, for consistency, the reported fluxes for the broad component of $H\beta$, $\text{Pa}\beta$, and $\text{Br}\gamma$ are compared to those reported by Landt et al. (2008) for the objects in common. We found the values agree within a factor of 2, with most cases the difference being not larger than 30 percent. Moreover, our measured fluxes for NGC 4151 and NGC 5548 are in excellent agreement to those reported by Landt et al. (2015a, b) for these two objects, respectively.

3 CORONAL LINE DIAGNOSTIC DIAGRAMS

The use of coronal lines as a proxy of black hole measurements was theoretically explored by Cann et al. (2018) via photoionization simulations. They show that for intermediate to low BH mass sources ($10^2\text{--}10^5 M_{\odot}$), CL of very high IP are favoured with respect to those of lower IP. Their approach, though, could not be assessed because of the lack of suitable data for AGNs with BH masses in that regime. Here, we expand the photoionization modelling to the high BH mass range $10^6\text{--}10^8 M_{\odot}$, and confront the predictions with the data gathered in Table 1.

Fig. 1 presents new diagnostic diagrams in which the BH mass for the objects in the sample is plotted against a given CL flux normalized to the closest in wavelength H I broad emission. The first plot – upper left panel, involving [Si VI] $1.9641 \text{ }\mu\text{m}/\text{Br}\gamma_{\text{broad}}$, IP [Si VI] = 167 eV, shows a clear trend with M_{BH} over three orders of magnitude in BH mass. A linear regression yields:

$$\log M_{\text{BH}} = (6.40 \pm 0.17) - (1.99 \pm 0.37) \times \log \left(\frac{[\text{Si VI}]}{\text{Br}\gamma_{\text{broad}}} \right), \quad (1)$$

and a 1σ dispersion of 0.47 dex in BH mass. The regression analysis follows the LTSFIT package³ (Cappellari et al. 2013), which accounts for the errors in all variables. The Pearson correlation coefficient is $r = -0.76$, with a null probability of $\text{Pr} = 3.8 \times 10^{-5}$.

A weak trend if any ($r = -0.5$) when involving [Fe VII], IP (100 eV), and no trend for the higher IP ($> 260 \text{ eV}$) CL [Si X] and [S VIII] are found. The correlation index for [S VIII]/ $\text{Pa}\beta_{\text{broad}}$ is $r = -0.44$, that for [Si X]/ $\text{Pa}\beta_{\text{broad}}$, is $r = -0.3$.

To construct these diagrams, several considerations were made. First, line ratios are chosen close in wavelength to minimize reddening. Secondly, the normalization of the CL emission is to the broad H I line, as only in this case the correlation ([Si VI]/ $\text{Br}\gamma_{\text{broad}}$) with

²Based on the Gemini IRAF packages

³<http://www-astro.physics.ox.ac.uk/mxc/software/lts>

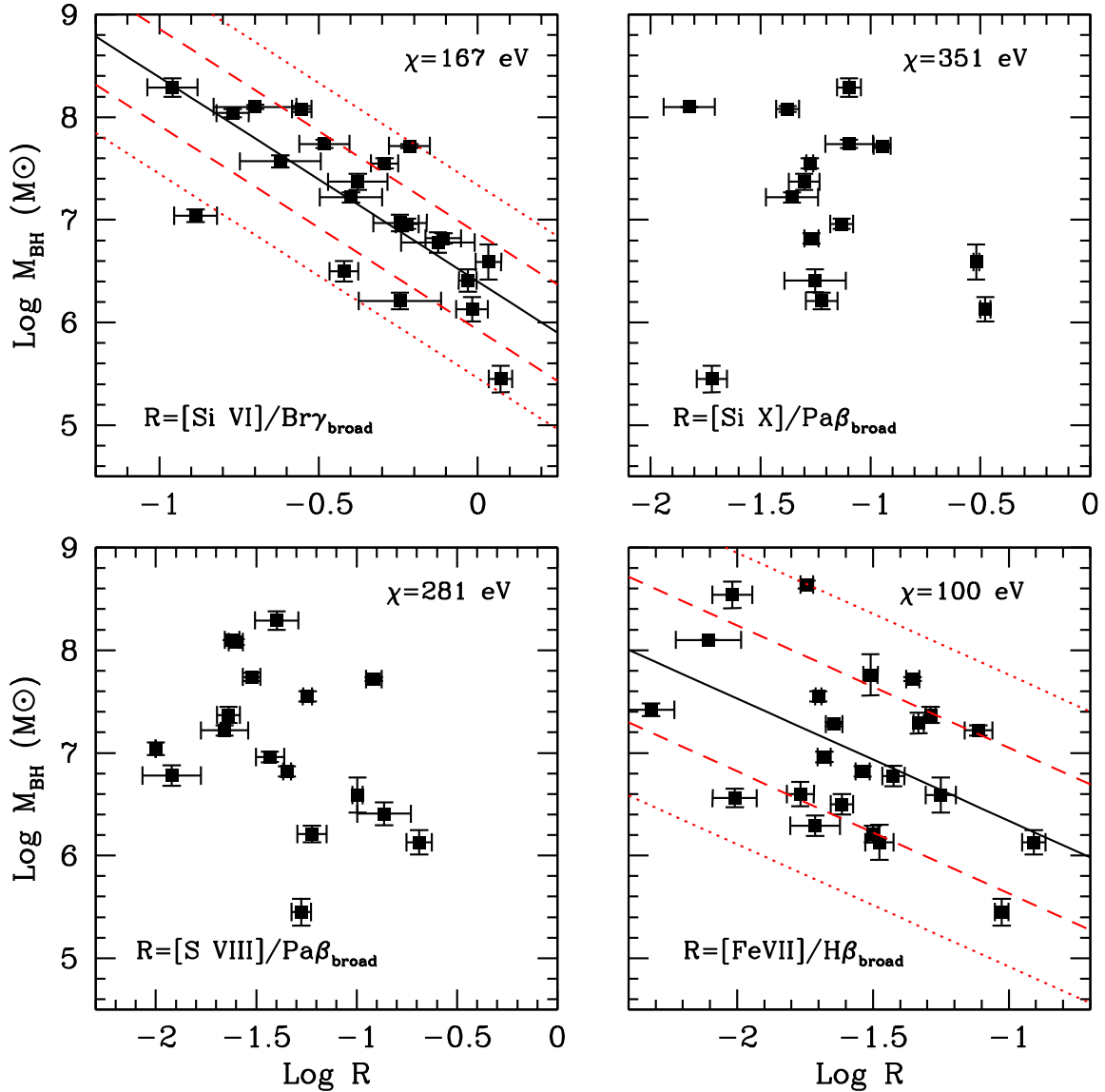


Figure 1. Observed CL emission normalized to the broad component of H II versus black hole mass for the objects in sample. The black line is the best-linear fit to the data and the red-dashed and dotted lines show the 1σ and 2σ deviation.

BH mass was found. Normalization to the H I narrow line emission was equally evaluated, yet not clear trend with BH mass could be recovered, the dispersion being too large. We believe that reasons for that are the much larger narrow-H I emitting volume as compared with that of the coronal region and the fact that H is subjected to additional ionization sources beside the AGN, e.g. star formation, whereas coronal gas is an unambiguous AGN tracer. The coronal gas is found in the inner parsecs of the central engine, at the boundary of the BLR clouds, as recently shown in spatially resolved observations of the broad and coronal clouds by GRAVITY Collaboration (2021). The CL high critical density, $n_e > 10^8 \text{ cm}^{-3}$, warrants its survival at the inner regions, possibly the nearest gas to the BLR – not at the BLR where densities are at least one order of magnitude higher. Hence, by normalizing to broad H I, the proposed CL ratios in this work become the closest possible tracer, perhaps a genuine one, of the conditions at the inner parsecs next to the accretion disc.

The derived correlation when involving the [Si VI] line over almost three order of magnitude in BH mass, the absence of an equivalent

dependence when involving the higher IP lines, prompted us to examine the impact of an accretion-disc continuum in the coronal gas production and, in turn, its dependence with disc temperature and BH mass.

The CL in Fig. 1 are sensitive to different energy ranges of the ionizing continuum. This is illustrated in Fig. 2, which shows a parametrization of an AGN ionizing continuum as a combination of a standard Shakura–Sunyaev (SS) accretion disc (Shakura & Sunyaev 1973), which accounts for the rising of the spectrum at UV-soft X-rays, and a power law with a low and high energy cut-off to account for the rising of the continuum at high energies. It follows the equation (CLOUDY C13.1 formalism is used – Ferland et al. 2013):

$$F_\nu = \nu^{\alpha_{uv}} \exp\left(\frac{-h\nu}{kT_{\text{disc}}}\right) \exp\left(\frac{-kT_{IR}}{h\nu}\right) + a\nu^{\alpha_x}. \quad (2)$$

The first term is the parametrization of the SS disc, represented by an exponential function with a cutoff at the disc effective temperature, T_{disc} , and a power law with $\alpha_{uv} = 0.33$ accounting for the low

energy tail of the disc. The low energy limit of the disc is set by the IR-exponential with cutoff at 0.01 Ryd. The high energy range is represented by a broken power law with spectral index $\alpha_x = -1$, and a cutoff at 100 keV. The scaling of the SS disc relative to the high energy power law is controlled by the parameter ‘a’ in equation (2), which refers to the ratio of the luminosities at 2 keV and at 2500 Å given by a power law with spectral index, so called α_{ox} , set here to -1.4 . With the exception of $\alpha_{uv} = 0.33$, all other parameters quoted above follow the generic AGN continuum used in CLOUDY C13.1– Section 6.2.

The IP of the CL and of H II are marked on the ionizing continuum, Fig. 2, to illustrate their both location and energy coverage in a typical AGN ionizing spectrum. They sample the bulk of the ionizing spectrum over the 13.6–351 eV energy range. The figure shows different SS accretion disc continuum for different BH masses and spin (see Section 4).

4 CORONAL EMISSION AS PROXY OF THE BLACK HOLE MASS

The peak emission in the ionizing continuum in Fig. 2 effectively samples T_{disc} , with the disc getting hotter as BH mass decreases as predicted by standard accretion disc theory. The IPs of the CL fall within the range of peak temperatures, closer or slightly further from the peak depending on BH mass. If the accretion disc is the main source of photons to ionize the coronal gas, a trend between CL strength and T_{disc} may be expected. Because of the dependence of T_{disc} with BH mass, a correlation between coronal line strength and BH mass may be ensued. This possibility is investigated below.

Following on the thin accretion disc approximation, for a Kerr BH, the disc T_{disc} can be approximated as (Frank, King & Raine 2002 formalism is used):

$$T_{\text{disc}} = 3.4 \times 10^5 K \left(\frac{M_{\text{BH}}}{10^8 M_{\odot}} \right)^{1/4} \times \left(\frac{dM/dt}{0.1} \right)^{1/4} \times \left(\frac{\eta}{0.26} \right)^{-1/4} \times \left(\frac{R_{\text{inG}}}{1.4} \right)^{-3/4}, \quad (3)$$

where, M_{BH} is the BH mass, (dM/dt) is the accretion rate in Eddington units, η is the BH accretion efficiency, R_{inG} is the innermost stable circular orbit in terms of the gravitational radius $R_G = GM_{\text{BH}}/c^2$ (G is the Gravitational constant, c is the velocity of light). The equation is normalized to $M_{\text{BH}} = 10^8 M_{\odot}$, accretion rate in Eddington units, $dM/dt \sim 0.1 (dM/dt)_{\text{Edd}}$, and a radiation efficiency, $\eta = 0.26$ corresponding to a BH spin of 99 per cent, i.e. $a = 0.99 GM_{\text{BH}}/c^2$ (hereafter $a = 0.99$), and co-rotation is adopted. Current estimates of BH spins from different methods point to values close to 1 (see Reynolds 2019, for a compilation). With increasing spin, the innermost stable orbit becomes smaller and T_{disc} increases accordingly. In the case of co-rotation, the disc temperature reaches the highest values.

The ionizing continua in Fig. 2 follow the $T_{\text{disc}} - \text{BH}$ mass approximation described in equation (3). Curves are presented for three different BH mass and two spin, 0.8 and 0.99. Spins below 0.8 produce a marginal difference in T_{disc} in comparison to the $a = 0.8$ case and are not shown (see e.g. Campitiello et al. 2019, for a spin parameter space study). It can be seen that the peak of the disc emission gets progressively closer to the IP of Si^{+5} and Fe^{+6} as we move down in BH mass, and increase spin. However, the accretion disc energies begin to fall short from those required for the higher IP ions, Si^{+9} and S^{+7} , when moving to the high BH masses, $10^7 - 10^8 M_{\odot}$, or higher – not shown – with T_{disc} becoming progressive cooler with increasing BH mass.

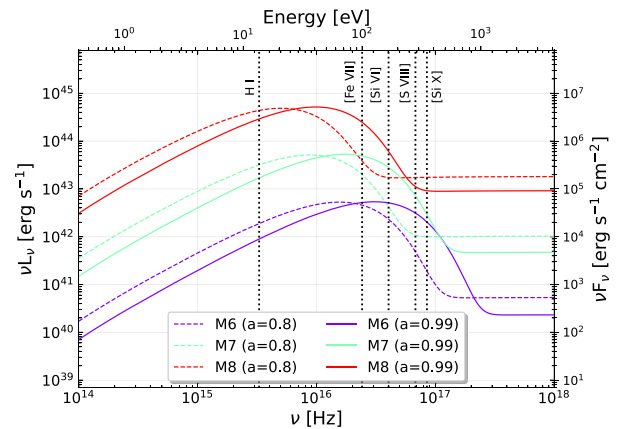


Figure 2. Generic AGN ionizing continuum used in this work as per equation (2) for the BH mass range in the AGN sample. Each curve corresponds to a BH mass with an associated T_{disc} following the SS disc approximation in equation (3). Two spin values, $a = 0.8$ (dashed curves) and $a = 0.99$ (solid curves), and three BH masses, i.e. M_{BH} (in units of M_{\odot}) = 10^6 (purple), 10^7 (green), and 10^8 (red) are shown. Vertical dashed lines mark the IPs of the lines used in the analysis.

On the above premises, a trend between T_{disc} and the excitation state of [Si VI] or [Fe VII] lines may be expected, whereas no trend involving the higher IP lines [Si X] or [S VIII] is foreseen. The high IP lines are, however, expected to be good proxies of the disc temperature for BH mass below $10^6 M_{\odot}$, as shown in the theoretical analysis by Cann et al. (2018). We believe that the expected CL emission dependence with disc temperature is a possible driver of the observed [Si VI] / $\text{Br}\gamma_{\text{broad}} - M_{\text{BH}}$ correlation, and may also explain the absence of an equivalent dependence for the higher IP [Si X] or [S VIII] lines. The hypothesis is tested in the next subsection with photoionization models.

We note also that contrarily to expectations, the trend with BH mass for the [Fe VII] case is weak, if any, even though the IP of Fe^{6+} is well sampled by the ionizing continua (Fig. 1). We are not yet understanding this result, but identify several observational issues that may affect the estimate of this CL ratio: 1) the high variability of $\text{H}\beta$ as compared with the much more stable near-IR Paschen and Brackett lines (Landt et al. 2011); 2) the continuum underlying broad $\text{H}\beta$, affected by a strong Fe II pseudo-continuum, makes difficult the estimate of broad $\text{H}\beta$; 3) differential reddening between $\text{H}\beta$ and [Fe VII]. None the less, this CL ratio is included in the photoionization modelling below.

4.1 Testing Coronal Line diagnosis diagrams with photoionization models

To probe the CL emission as a proxy of the disc temperature, we make use of the photoionization code CLOUDY (v17.02 Ferland et al. 2017). The goal is to test whether the CL line ratios used in Fig. 1 show a dependence with T_{disc} , this being an input to CLOUDY via the ionizing continua shown in Fig. 2. A range of electron densities, n_e , and cloud distances to the centre, r , in line with CL observations are input to CLOUDY. These parameters are selected as follows.

Coronal gas extends at most up to a few tens of parsec (Prieto et al. 2005). The bulk of the emission is mostly nuclear (Müller-Sánchez et al. 2011), spreading over sub-parsec scales (e.g. Gravity Collaboration 2020; GRAVITY Collaboration 2021) and can be explained by photoionization (e.g. Ferguson et al. 1997; Contini & Viegas 2001; Rodríguez-Ardila et al. 2006). For the present test, the bulk of CL in

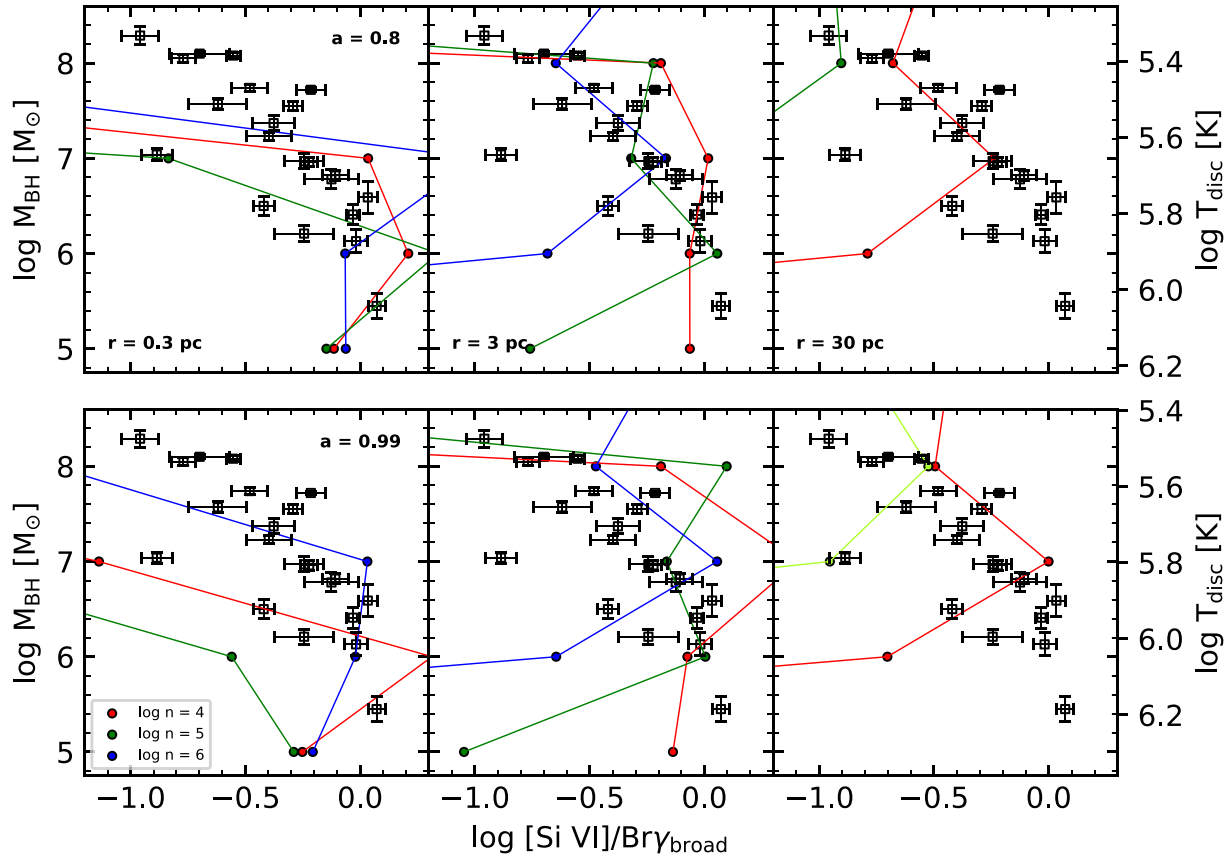


Figure 3. CLOUDY predictions for $[\text{Si VI}]/\text{Br}\gamma_{\text{broad}}$ versus BH mass using as ionizing continuum equation (2). Models are run for densities $n_e = 10^3 \text{ cm}^{-3}$ in red, 10^5 cm^{-3} (green) and 10^6 cm^{-3} (blue). Each subplot shows the model results for distance r to the ionizing source, $r = 0.3, 3,$ and 30 pc , depicted from left to right. Two spins, $a = 0.8$ (upper panel) and $a = 0.99$ (lower panel) are considered. The corresponding T_{disc} per each BH mass – after equation (3) – are depicted on the y-axis, right-side. Data points as in Fig. 1 are black squares.

the sample is assumed to be nuclear and powered by photoionization from the accretion disc. Spatially resolved nuclear CL by GRAVITY interferometry reveals the coronal region extending up to 0.3 pc from the centre. Thus, a range of r between 0.3 and 30 pc are tested.

Gas densities, n_e , in the $10^4 \leq n_e \leq 10^7 \text{ cm}^{-3}$ range are probed, the upper limit set by the critical density of the CL probed – $n_e > 10^8 \text{ cm}^{-3}$, the lower limit is set by the average densities inferred from the mid-IR $[\text{Ne V}]$ lines, $\text{IP} = 97 \text{ eV}$, $10^3 - 10^4 \text{ cm}^{-3}$ (e.g. Moorwood et al. 1996; Fernández-Ontiveros et al. 2016).

The input ionizing continuum is set by the equation (2; Fig. 2), normalized to an adopted value of $L_{\text{bol}}/L_{\text{Edd}} = 0.1$. The present sample covers a range of Eddington ratio in the range $0.01 \lesssim L_{\text{bol}}/L_{\text{Edd}} \lesssim 0.2$ as reported in the literature. These values are none the less subject to uncertainties up to an order of magnitude due to the evaluation methods and assumptions made to estimate L_{bol} (see e.g. Richards et al. 2006). For a few sources, reliable L_{bol} are available from integrating the parsecs-scale SED (e.g. Prieto et al. 2010). This is the case for NGC 7469 and NGC 3783, for which $L_{\text{bol}}/L_{\text{Edd}}$ are 0.25 and 0.06, respectively. A few other sources have L_{bol} estimated from hard X-ray data (Winter et al. 2012), re-normalizing the Eddington ratios inferred by these authors to the BH masses in Table 1, yields $L_{\text{bol}}/L_{\text{Edd}}$ in the $0.01 - 0.1$ range. For the present test, a nominal $L_{\text{bol}}/L_{\text{Edd}} = 0.1$ is adopted, in line with the median found in larger quasar distributions, such as the SDSS DR7 quasar catalogue (Shen et al. 2011; Panda et al. 2018). The impact of changing $L_{\text{bol}}/L_{\text{Edd}}$ in the model results is discussed in next section.

4.2 Predictions versus observations

Figs 3–6 show CLOUDY predictions for the CL ratios in this work as a function of T_{disc} (in the right axis), and of BH mass (on the left axis, following the transformation in equation 3 for $L_{\text{bol}}/L_{\text{Edd}} = 0.1$). Models are shown for a range of densities, $10^4 \leq n_e \leq 10^6$, clouds distance to the centre, $0.3 \text{ pc} \leq r \leq 30 \text{ pc}$, and two spins, 0.8 and 0.99 – following discussion in Section 4.1. Given the BH spin, the two left free parameters in equation (3), accretion efficiency (η) and the location of the innermost stable circular orbit R_{inG} , are set uniquely.

As discussed, the CL data is normalized to H I broad emission. Yet, CLOUDY predictions are derived for densities at least two orders of magnitude below that of the broad-line region to cope with the lower CL critical densities. Thus, in comparing both a caveat is introduced, which mainly relates to the different volume emissivity of H I in the broad and in the coronal line region. To account for the difference a correction factor was required to shift CLOUDY line ratio predictions on top of the plotted ratios. We find a factor of 15 as best compromise to get the predicted $[\text{Si VI}]/\text{Br}\gamma$, for the whole range of n_e , r , and spin considered, on top of the plotted $[\text{Si VI}]/\text{Br}\gamma_{\text{broad}}$ data. Having fixed the scale factor for this ratio, the scaling for the other CL ratios were derived by imposing theoretical H I recombination ratios. Accordingly, a factor of 25 is applied to CLOUDY’s $[\text{Fe VII}]/\text{H}\beta$, and 90 for both $[\text{S VIII}]/\text{Pa}\beta$ and $[\text{Si X}]/\text{Pa}\beta$. CLOUDY models in Figs 3, 4, 5, and 6 are all shifted in the X-axis by these factors.

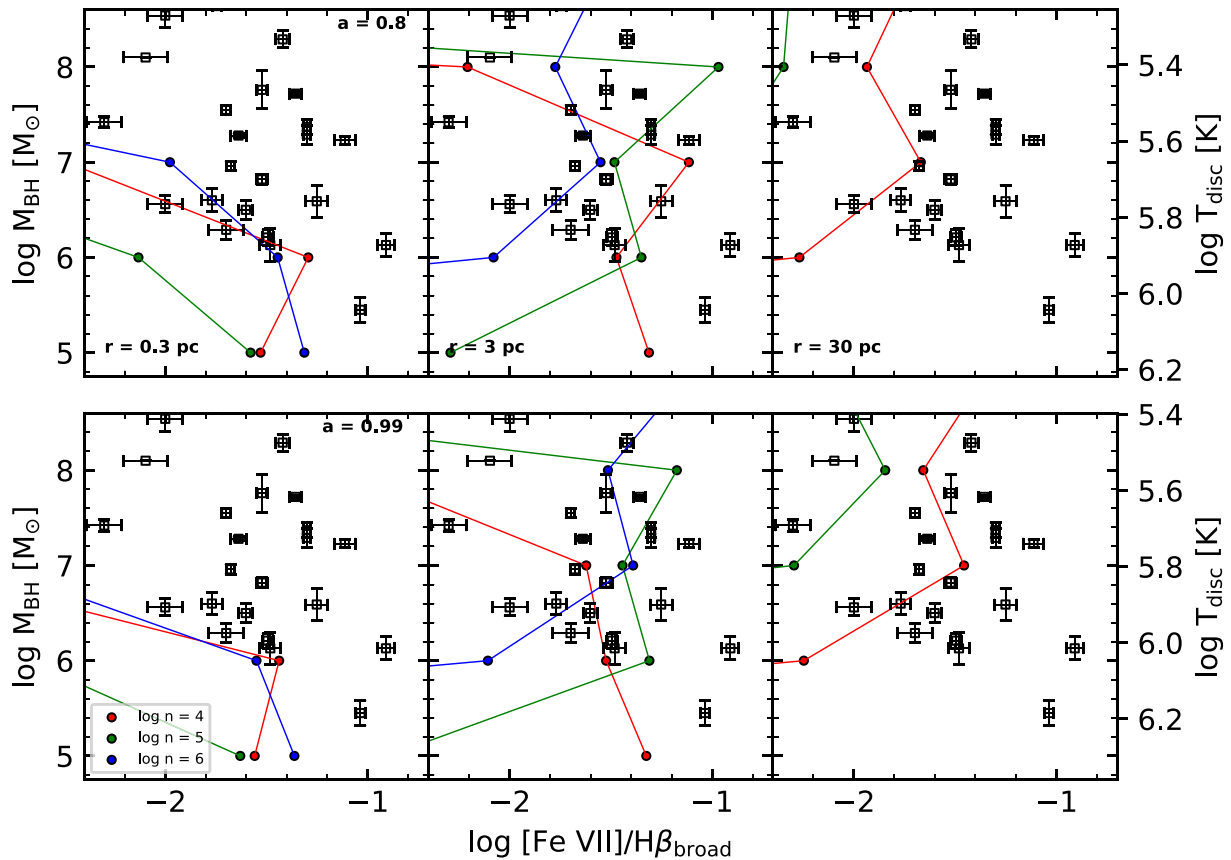


Figure 4. As in Fig. 3 but for $[\text{Fe VII}]/\text{H}\beta_{\text{broad}}$.

Focusing on the results for $[\text{Si VI}]/\text{Br}\gamma_{\text{broad}}$, Fig. 3, the models that best account for the whole range of observed ratios and their trend with BH mass are for cloud distances, r , of 3 pc and densities in the range $10^5 - 10^6 \text{ cm}^{-3}$ (middle panels). The case of spin 0.8 gives the best match, the spin 0.99 case provides an envelope of the scatter in the data. Models with cloud distances higher or lower than $r = 3 \text{ pc}$ are more restrictive in covering the whole range of CL ratios, or BH mass. Models with distances as large as $r = 30 \text{ pc}$ provide a fair account of the trend for the larger BH masses provided the densities are in the lower range as expected for clouds at those large distances. This model none the less is presented as a limit case as in the present context, the CL to BL emission comparison may not be applicable. Models for $r = 0.3 \text{ pc}$ provide moderate account for the lowest mass range. Overall, no single model reproduces the whole range of observed CL ratios, but changes in cloud density appear to reproduce the general $[\text{Si VI}]/\text{Br}\gamma_{\text{broad}}$ versus BH mass trend particularly for $r = 3 \text{ pc}$. The observed correlation shows an scatter of 0.47 dex (Fig. 1, Section 3), and part of it should be intrinsic, reflecting the different physical properties of the objects in the sample in terms of spin, and accretion rate – evaluated below – and also the CL region both density and distance to the centre.

Focusing on $[\text{Fe VII}]/\text{H}\beta_{\text{broad}}$, the observations show a rather scatter dependence with BH mass (Fig. 4).

It is noteworthy though that the models that best account for the data spread are those that best account for the $[\text{Si VI}]$ ratio trend, the $r = 3 \text{ pc}$ models. All other models provide a poor representation of the loci of the data. The fact that a favoured model, $r = 3 \text{ pc}$, is hinted for both $[\text{Fe VII}]$ and $[\text{Si VI}]$ line ratios is somewhat expected given that the IP of both lines sample properly T_{disc} for the range of BH

mass considered (Fig. 2). It is also interesting that for the $[\text{Fe VII}]$ case, the models show an also erratic dependance with BH mass as do the data that contrasts with the better behaved trend shown for the $[\text{Si VI}]$ line case. This result and particularly the observational one need to be further explored.

Regarding the higher IP CL ratios $[\text{Si X}]/\text{Pa}\beta_{\text{broad}}$ and $[\text{S VIII}]/\text{Pa}\beta_{\text{broad}}$, as discussed in Section 4, none of the two show a dependance with BH mass. None of the tested models, included the favoured one $r = 3 \text{ pc}$ even account for the loci of the data, with the exception of the $r = 0.3 \text{ pc}$ case (left-hand panels in both Figs 5 and 6). In the context of the present analysis, this result is what is expected for two reasons: 1) the lack of a dependence of BH mass with T_{disc} for these CLs is attributed to their IP falling at the high energy end of the disc spectrum (Fig. 2), hence T_{disc} is not as well sampled as for the case of lower IP CL for the range of BH mass considered. The lack of dependence with T_{disc} is also indicated by the CLOUDY predictions, particularly for the $[\text{S VIII}]/\text{Pa}\beta_{\text{broad}}$ case which shows an almost straight line along the temperature axis, as do the data, whereas a more erratic behaviour is predicted for the $[\text{Si X}]$ case, as also seen the data; 2) the higher IP of $[\text{S VIII}]$ and $[\text{Si X}]$ naturally leads to the formation of these ions at the innermost edge of the CL region, hence, models with r closer to the central engine should be favoured, as it appears to be the case. It may also be considered to decrease the density to foster the production of these ions at larger r , yet, this severely penalizes the line emissivity, proportional to ne^2 , as it can be inferred from the results (Figs 5 and 6).

We finally test the impact of an accretion rate different from the standard 10 per cent Eddington used in the models above. An evaluation of the $L_{\text{bol}}/L_{\text{Edd}}$ for some of the objects in the sample

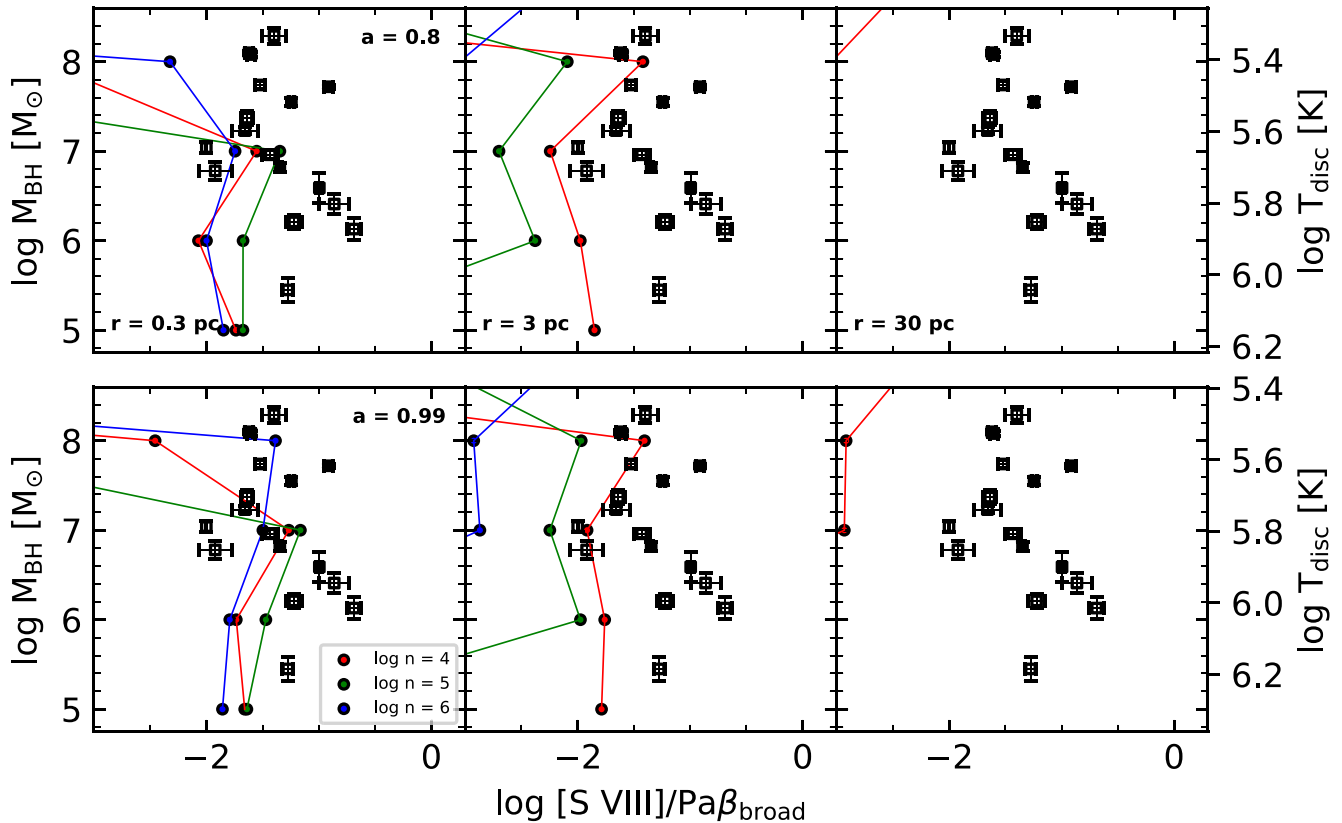


Figure 5. Similar to Fig. 3 but for $[\text{S VIII}]/\text{Pa}\beta_{\text{broad}}$.

points to a range between 1 per cent and a few 10 per cent (Section 4.1). Narrow Line Seyferts type-I are also predicted to have high Eddington ratios (e.g. Kuraszkiewicz et al. 2000; Panda, Marziani & Czerny 2019). Decreasing $L_{\text{bol}}/L_{\text{Edd}}$ to 1 per cent lowers T_{disc} normalization in equation (3) by factor ~ 1.8 , which is about the same factor reduction introduced by change of spin from 0.99 to 0.8. The net effect in the models would be equivalent to that produced by the change of spin shown in all the figures, Figs 3–6. Effectively, the decrease in T_{disc} implies CL ratios progressively smaller, but the trend of the models keeps similar particularly for cloud distances $r \gtrsim 3$ pc. Conversely, increasing $L_{\text{bol}}/L_{\text{Edd}}$ would shift the models in opposite direction towards higher T_{disc} . An increase in Eddington ratio by factor 3 yields an increase in T_{disc} by 1.3. Focusing on the $[\text{Si VI}]/\text{Br}\gamma_{\text{broad}}$ versus BH mass correlation, lowering (increasing) the accretion rate or spin just provide the envelope to enclose the scatter of the data. The dispersion in the observed correlation could largely be attributed to the range of spin and Eddington accretion rate in the sample.

4.3 Testing the relative-contribution / shape of the soft X-rays component on coronal emission

4.3.1 Modifying α_{ox}

The IP of the CLs in this work extends over the soft X-rays, spreading over the 100–350 eV range. The generic ionizing continuum used up to now (equation 2, Fig. 2), is sampled with an SS disc joined with a power law at the high energies whose relative contribution is fixed with the α_{ox} parameter set to -1.4 . Obviously the contribution of the hard energy spectrum, which is modulated by this parameter, affects

in different degrees the CL production, particularly for the highest IP lines. This effect is evaluated below.

α_{ox} in AGN falls in the -1.0 to -2.0 range (Avni & Tananbaum 1986; Wilkes et al. 1994; Lusso & Risaliti 2017), with a typical value about -1.4 (Zamorani et al. 1981; Ferland et al. 2013). A new set of models are evaluated using the generic ionizing spectrum in equation (2) normalized to either $\alpha_{\text{ox}} = -1$ or -2 . To make the comparison with previous results simple, a reduced set of parameters that best account for both the $[\text{Si VI}]$ ratio – BH mass correlation and the data loci in the $[\text{Fe VII}]$ ratio versus BH mass are tested, namely $r = 3$ pc, spin = 0.8, and density = 10^4 cm^{-3} (Section 4.2). The results are in Fig. 7, along with the default $\alpha_{\text{ox}} = -1.4$ model case in Figs 3–5. It can be seen that the $\alpha_{\text{ox}} = -1.4$ case still provides the best envelope of the $[\text{Si VI}]$ CL ratio versus BH mass correlation – note that one single density is shown. The new models miss the trend of the data particularly for BH mass above $10^{6.5} M_{\odot}$. No major impact is seen for the $[\text{Fe VII}]$ ratio versus BH mass case, nor for the higher IP lines as compared with the default case. Summarizing, making harder / softer the contribution of the high energy spectrum in the ionizing spectrum does not lead to a better or different account of the data as compared with the compromise case, $\alpha_{\text{ox}} = -1.4$.

4.3.2 Adding a warm Comptonization component

A soft X-rays excess below ~ 1 keV on top of the nominal high energy power-law spectrum is often feature in AGN spectra, with NLS1 being the most clear representatives (cf. Boller, Brandt & Fink 1996). Its origin has been interpreted as reprocessed emission from the hot disc corona or as an additional warm Comptonizing component

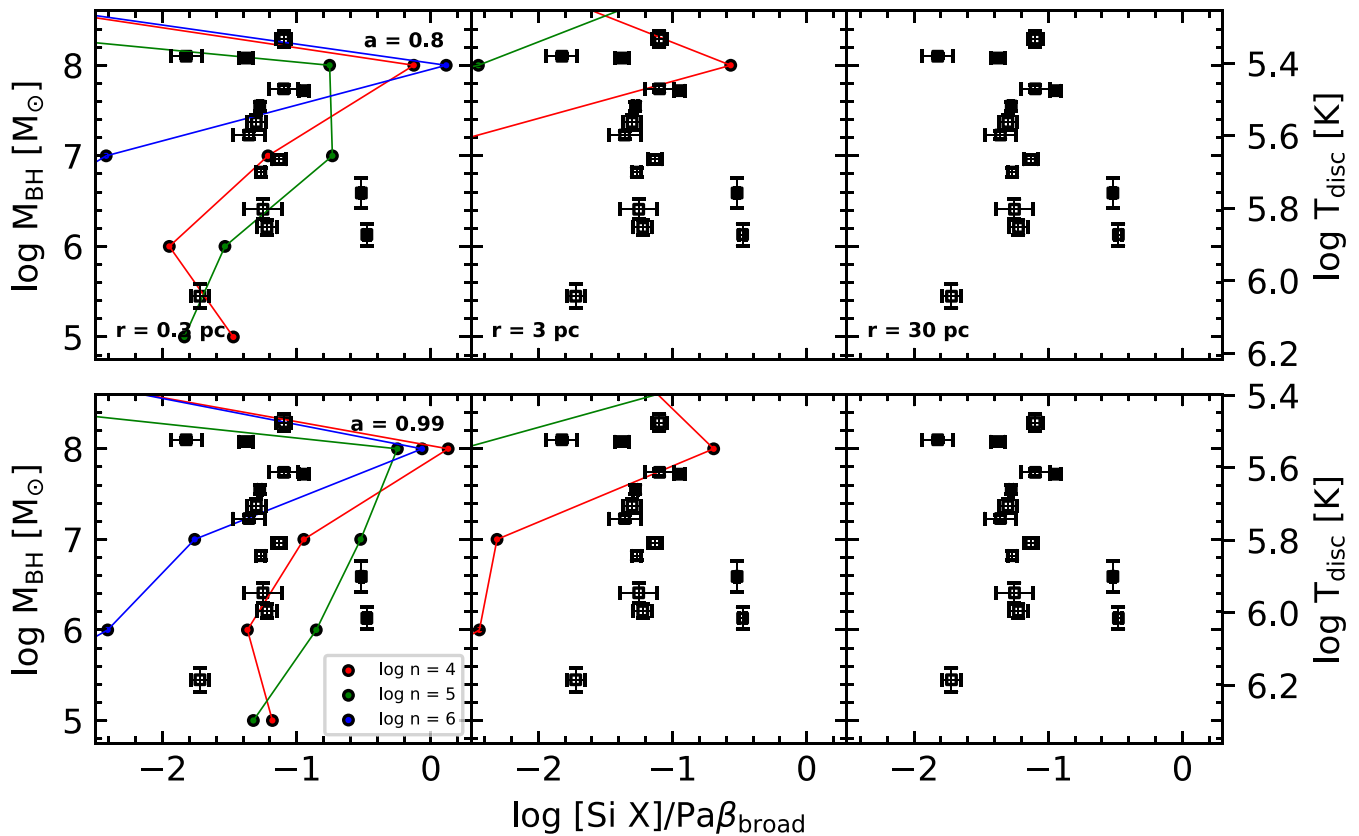


Figure 6. Similar to Fig. 3 but for $[\text{Si X}]/\text{Pa}\beta_{\text{broad}}$.

dominating the soft X-rays (e.g. Fabian et al. 2013; Kubota & Done 2018, and references therein).

For the purpose of this work, to assess the effect of an additional soft X-ray excess component in the generic AGN ionizing continuum in this work – equation (2), the warm corona component as described in Kubota & Done (2018) is taken as a reference and incorporated as additional component to the generic continuum. The warm corona models are extracted from AGNSED model (Kubota & Done 2018) using XSPEC (Arnaud 1996). The new ionizing continuum is shown in Fig. 8 along with the generic one, equation (2), used in this work. The new model is calculated for Eddington accretion rate of 10 per cent, as the generic case, but only the spectrum for spin = 0.8 is shown. In comparing both spectrum, it can be seen in the figure that with the addition of the warm component the peak of the ionizing continuum moves toward cooler temperatures. And because of the new shape of the spectrum, the IP of the CLs, particularly of the reference ones, $[\text{Si VI}]$ and $[\text{Fe VII}]$, fall in a region of the spectrum rather flat with little change with BH mass.

Fig. 9 shows the new model results for the four CL ratio versus BH mass relations tested in this work. As in Section 4.3.1, models are run for a restricted parameter range, i.e. $n_e = 10^4 \text{ cm}^{-3}$, $r = 3 \text{ pc}$, and spin $a = 0.8$, with all other parameters as in the generic case (Section 4.1), included α_{ox} set to -1.4 .

The new models provide rather similar behaviour in CL ratio versus BH mass as those produced with the change of α_{ox} . The inclusion of the warm soft component predicts lower values for the $[\text{Si VI}]$ - and $[\text{Fe VII}]$ - ratios, as compared with the effect of changing α_{ox} , but otherwise the generic ionizing continuum still provides the best envelope of the observed $[\text{Si VI}]$ ratio versus BH mass relation.

Not major impact is found for the $[\text{Fe VII}]$ versus BH mass diagram, if any the BH mass range is slightly better covered by the generic model. Results are very similar among all models regarding the high IP CL ratios versus BH mass diagrams. Either the range of CL ratios or of BH masses are poorly covered in all cases. There are two aspects to emphasize here. 1) as discussed in Section 4.2 the high IP CL ratios show no dependence with BH mass, nor any of the generic models hinted for a dependence either. It was argued as possible cause the high IP of the lines which are barely sampled by the SS disc for the range of BH mass considered. It is not surprising finding similar result with the new soft X-ray enhanced ionizing continuum because of the flattening of spectrum at the relevant energies region for all the BH masses. 2) the new models are run for CL cloud distances $r = 3 \text{ pc}$ whereas smaller r cover best the bulk of the data as found with the generic ionizing continuum (best coverage is found for $r = 0.3 \text{ pc}$, Section 4.2). Yet, because of 1) models for $r = 0.3 \text{ pc}$ will not provide a distinct result from that obtained with the generic case.

5 OVERALL VIEW: A CORONAL GAS–BH MASS CALIBRATION

Using *bona-fide* BH mass estimate from reverberation mapping and the line ratio $[\text{Si VI}] 1.963 \mu\text{m}/\text{Br}\gamma_{\text{broad}}$ as a genuine tracer of the AGN ionizing continuum, a BH-mass scaling relation over almost three orders of magnitude in BH mass, 10^6 – $10^8 M_{\odot}$, is found (Fig. 1). The dependence follows a linear regression in log scale $M_{\text{BH}} \propto ([\text{Si VI}]/\text{Br}\gamma_{\text{broad}})^{1.99 \pm 0.37}$, with a dispersion in BH mass of 0.47 dex (Section 3). Following on the thin accretion disc approximation and after surveying a basic parameter space for coronal gas production, we believe one of the key parameters driving

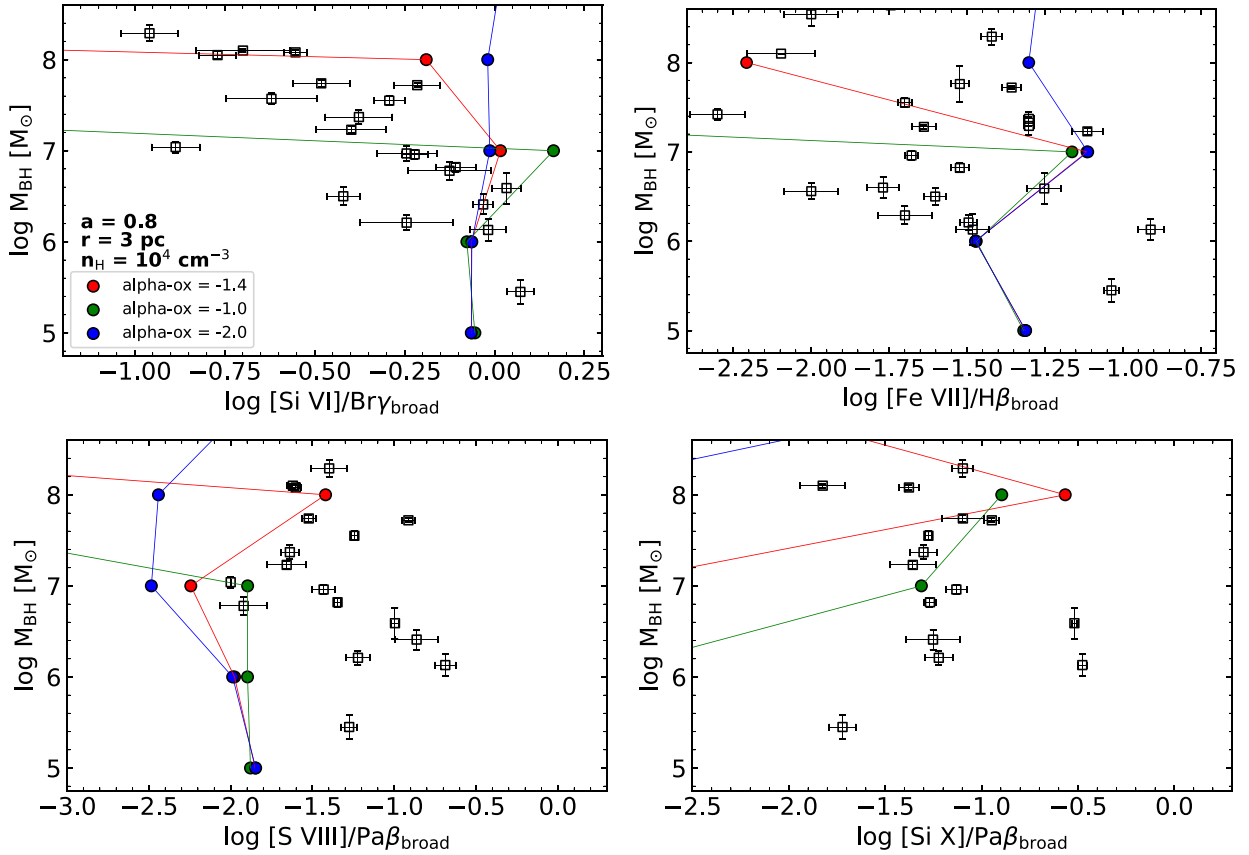


Figure 7. CLOUDY predictions for the four CL ratio versus BH mass diagrams in this work. The ionizing continuum is that of equation (2) but for different values of α_{ox} : red refers to $\alpha_{\text{ox}} = -1.4$ – default value used in this work, Section 4.2 – green for $\alpha_{\text{ox}} = -1$, blue for $\alpha_{\text{ox}} = -2$. Models are run for a suit of parameters that best account for the [Si VI] – BH mass correlation (Fig. 3): density $n_e = 10^4 \text{ cm}^{-3}$, distance $r = 3 \text{ pc}$, spin $a = 0.8$. All other parameters are in the default case. Data points as in Fig. 1 are black squares.

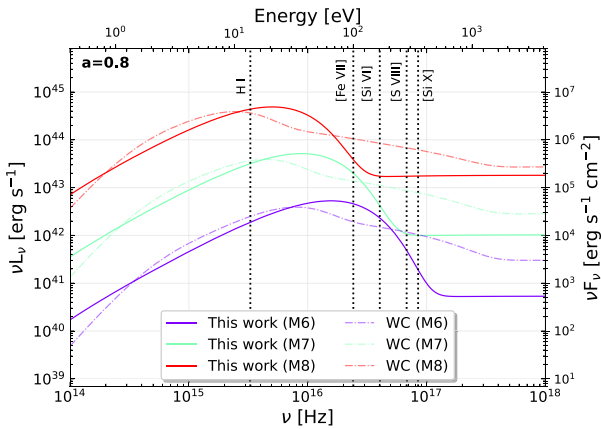


Figure 8. Generic AGN ionizing continuum as per equation (2) with the addition of a Warm Comptonizing component (WC in dashed line, following prescription by Kubota & Done 2018; Section 4.3.2). The generic case for spin 0.8 (Fig. 2) is shown for comparison in solid line (note that the spin 0.8 case in Fig. 2 is shown instead with a dots line). As in Fig. 2, each case is shown for three BH masses, but one spin, $a = 0.8$. All curves are normalized to $L_{\text{bol}}/L_{\text{Edd}} = 0.1$. Vertical lines mark the IPs of the lines used in the analysis.

this correlation is the effective temperature of the accretion disc, the correlation being formally in line with the thin disc prediction $T_{\text{disc}} \propto M_{\text{BH}}^{-1/4}$.

On these bases, on the assumption of a thin disc as the dominant component of the ionizing continuum (Fig. 2), and a suitable range of densities $n_e \sim 10^4\text{--}10^6 \text{ cm}^{-3}$ and cloud distances, $0.3 < r < 30 \text{ pc}$, for CL survival, photoionization models provide a fair representation of the M_{BH} and [Si VI]/ $\text{Br}\gamma_{\text{broad}}$ correlation.

No correlation is recovered when normalizing the CL emission to narrow H I gas. This may be due to two facts: 1) the much larger emission region covered by H I as compared with that from CL gas; 2) H I may be subjected to additional ionization sources other than the AGN which is not the case for CL gas. However, the normalization to broad H I introduces a complication when comparing with photoionization models, these been evaluated for narrow H I gas. To account for this difference, a scaling factor between broad-measured and narrow-predicted H I gas is introduced. This scaling factor should be understood as a way to account for the different volume emissivity and density that characterize the Broad- and the Coronal- line region. This scaling factor was found in an interactive form, by shifting the models predictions for [Si VI]/ $\text{Br}\gamma_{\text{broad}}$ on top of the observed ratios normalized to $\text{Br}\gamma_{\text{broad}}$. A factor around 15, unique for all models and objects in the sample, is found as the best compromise for this CL ratio. All other CL – H I-broad ratios

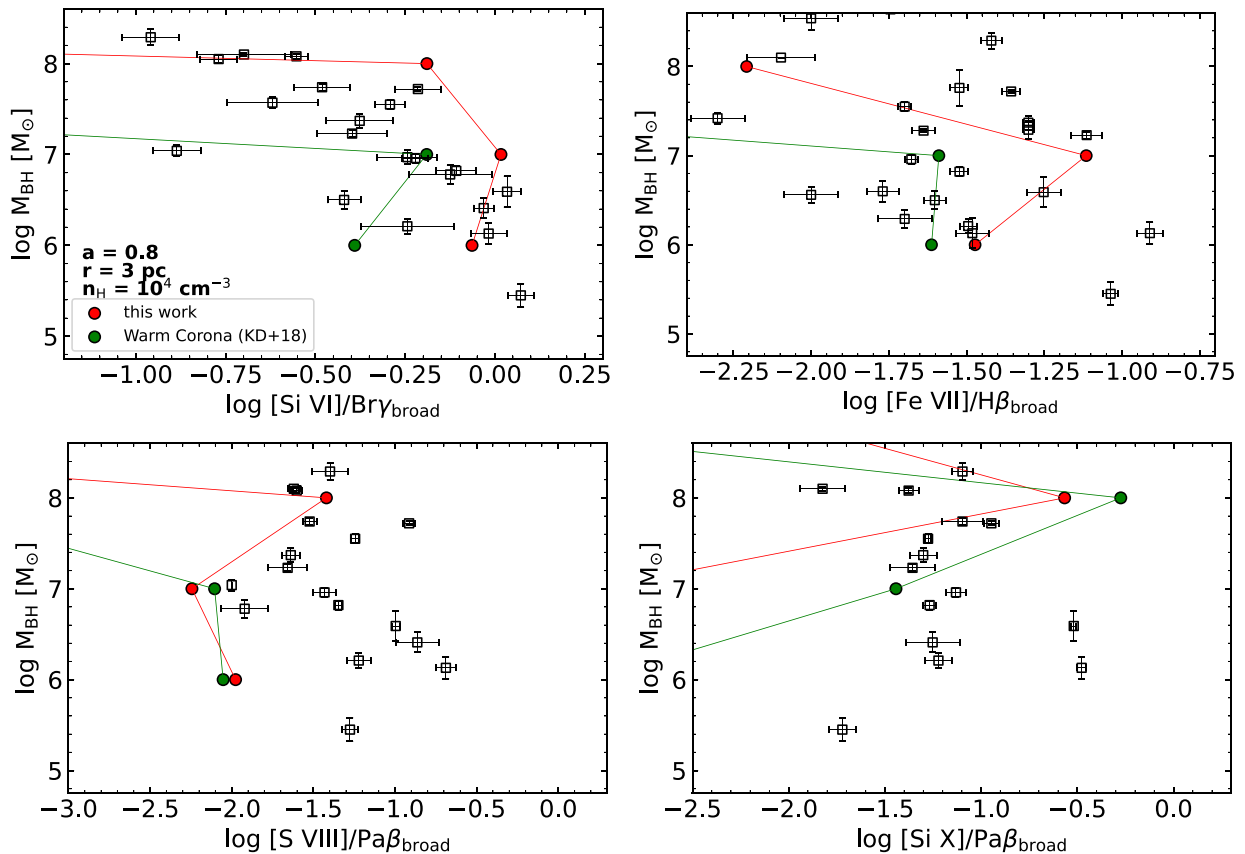


Figure 9. CLOUDY predictions for the four CL ratio versus BH mass diagrams in this work. In green is shown the case for the generic ionizing continuum with the addition of a warm X-ray component (Section 4.3.2); in red is the default generic case. Model parameters are as in Section 4.3.1 case: $n_e = 10^4 \text{ cm}^{-3}$, $r = 3 \text{ pc}$, spin $a = 0.8$, $\alpha_{\text{ox}} = -1.4$ with rest of parameters as in Section 4.1. Data points as in Fig. 1 are black squares.

used in this work were consequently scaled down from that factor following recombination values.

No correlation involving the higher IP lines, [Si x] and [S VIII], IP $> 250 \text{ eV}$ is seen (Fig. 1). We believe this a natural consequence of the $T_{\text{disc}} - \text{BH mass}$ dependence. Higher IP lines sample hotter discs, as compared with the [Si VI] IP, and in turn smaller BH masses, not covered by this sample, hence the absence of a positive trend for the range of masses in this work. It follows that a lack of dependence with T_{disc} should then be expected. This is consistent with the photoionization predictions as inferred from the same set of models used for the [Si VI] case (Figs 5 and 6). The high IP CL are, however, expected to show a dependence with BH masses below $10^6 M_{\odot}$ (Fig. 2, equation 3), making them suitable BH mass scaling indicators for intermediate BH masses, as suggested by Cann et al. (2018). Testing this low mass end is currently limited due to the unavailability of accurate BH masses and suitable CL data.

Thus, the BH mass – CL dependence appears sensitive to the ionization potential of the CL employed. The use of [Si VI] $1.963 \mu\text{m}$, IP = 167 eV, restricts the dependence to BH masses in the range $10^6 - 10^8 M_{\odot}$, presumably because of the disc temperature, for these masses, favours the production of Si^{+5} best (Fig. 2). In the same line of reasoning, an equivalent dependence involving other CL with IP close to the disc peak emission for these range of BH mass should be expected. Such is the case of e.g. [Fe VII] $\lambda 6087\text{\AA}$, IP = 100 eV, but a scatter relation is found instead. Photoionization predictions do not hint for a dependence with Temperature either (Fig. 4). Thus

no clear conclusion for the potential of this line as gas temperature can be assessed.

Other suitable CL are those of Ne^{+4} IP = 97 eV. Yet, the UV lines are much subjected to reddening, those in the mid-IR are optimal but available for few sources with accurate BH mass determination. The analysis of these few sources shows indeed a trend with BH mass but the statistic is insufficient to establish a correlation, the analysis is in progress.

Above $10^8 M_{\odot}$ BH mass, disc temperatures are foreseen in the 10^5 K regime in the disc approximation. Lower ionization lines would then be more favoured than the higher ones. The [Si VI]/ $\text{Br}\gamma_{\text{broad}}$ BH mass correlation points in that direction, with [Si VI]/ $\text{Br}\gamma_{\text{broad}}$ decreasing with increasing BH mass (Fig. 1). The high BH mass tail in the local Universe is the realm of elliptical and bulge dominated objects often associated with LINER (Low Ionization Nuclear Emitting Regions) activity. The parsec-scale spectral energy distribution of some of these sources strictly limit the temperature of the disc to $< 10^5 \text{ K}$ (Fernandez-Ontiveros et al. in preparation). Parsec-scale near-IR observations have so far proven the elusiveness of CL emission in a few of these cases (Müller-Sánchez et al. 2013; Mazzalay et al. 2014), in line with that prediction. These sources would appear as upper limits at the high mass range in Fig. 1.

Because of the different physical properties of the objects in the sample, some of the scatter in the proposed BH mass scaling relation should be intrinsic. In the proposed scenario, prime properties that should differ between objects are the accretion rate and spin. They affect the observed CL ratios dependence with BH mass in different

degrees. Best agreement with the observed $[\text{Si VI}] 1.963\mu\text{m}/\text{Br}\gamma_{\text{broad}} - \text{BH}$ mass trend is achieved for spins above 80 per cent and Eddington accretion rate of 10 per cent (Fig. 3). An increase in spin, or decrease in accretion rate, translates into a similar effect, namely a progressive shift to higher, or lower, T_{disc} for same BH mass, by factor of about 1.8 from spin = 0.8–0.99 or Eddington accretion rate from 10 per cent to 1 per cent (Fig. 3). Higher Eddington rates up to 30 per cent, in line with some objects in the sample, would lead to a slight increase in T_{disc} by 1.3. In practice, the decrease in T_{disc} makes $[\text{Si VI}]/\text{Br}\gamma$ progressively less sensitive to lower BH mass as the peak temperature of the disc moves away from the optimal energy for producing Si^{+5} , whereas the increase in T_{disc} by similar factor would favour the diagnosis for lower BH masses.

Finally, changes on the relative contribution of a soft X-ray excess component on the CL ratio – BH mass dependences was evaluated. This was done by either changing the α_{ox} parameter or adding a warm X-ray corona component in the standard ionizing continuum used in this work. None of these variants provide a significative account of the BH mass – $[\text{Si VI}]$ ratio correlation (Fig. 7, 9). Nor a significant result was found for the higher IP CLs, this even though the modification of the ionizing spectrum at the relevant energies to produce these lines. An important result from the photoionization modelling is that to produce the range of CL ratios observed at these high IPs, clouds should be less than few tenth of parsec from the centre (Figs 5 and 6). Still, to verify the potential of these high IP lines as BH mass scale tracers, the lower BH mass range has to be tested. The detection of coronal $[\text{Fe X}]$, IP = 240 eV, in a large sample of dwarf galaxies by Molina et al. (2021) opens an exciting avenue.

With a final compendium of 21 objects, the dispersion in BH mass in the proposed calibration is 0.47 dex (1σ). In comparison, a dispersion of 0.44 dex is inferred from the $M-\sigma$ relation in 49 galactic bulges with direct dynamical BH mass estimate (Gültekin et al. 2009). The intrinsic scatter in the mass – luminosity relations is in the 40 per cent range (Kaspi et al. 2005), mostly driven by differences in optical – UV continuum shape. In the present $[\text{Si VI}] - \text{BH}$ mass correlation, variations in the ionizing continuum shape e.g. the soft X-ray excess slope and contribution should contribute to the scatter but we consider that a minor effect as the production of the CL gas is mostly driven by the peak energy in the UV.

The present BH mass scaling relation is restricted to Type 1 AGN including narrow line Type I. The limitation is driven by the imposition of including *bona-fide* BH masses only, and the need to normalize to broad H I gas. We are none the less examining possibilities to extend it to Type 2. Source variability or changes in instrumental setup are not an issue. We found that most of the scatter is chiefly driven by differences in BH spin and accretion rate. The new scaling offers an economic, and physically motivated alternative for BH estimate using single epoch spectra, avoiding large telescope time (reverberation mapping) or absolute flux calibration (the continuum luminosity method). With James Webb Space Telescope and big surveys in the IR region, large samples of AGNs could be weighted using this approach.

ACKNOWLEDGEMENTS

We are grateful to the referee, Hermine Landt, for her positive suggestions to improve this manuscript. We are grateful to H. Netzer, E. Churazov, B. Czerny, A. Askar for discussions. AP thanks the support of the Excellence Cluster ORIGINS which is funded by the Deutsche Forschungsgemeinschaft (DFG, German Research Foundation) under Germany Excellence Strategy - EXC-2094 - 390783311. A.R.A acknowledges partial support from CNPq

Fellowship (312036/2019-1 & 203746/2017-1). SP acknowledges partial support from the Polish Funding Agency National Science Centre, project 2017/26/A/ST9/00756 (MAESTRO 9) and the computational facility at Nicolaus Copernicus Astronomical Centre.

DATA AVAILABILITY

Data products will be shared on reasonable request to the corresponding author.

REFERENCES

- Abazajian K. N. et al., 2009, *ApJS*, 182, 543
 Arnaud K. A., 1996, in Jacoby G. H., Barnes J., eds, ASP Conf. Ser. Vol. 101, Astronomical Data Analysis Software and Systems V. Astron. Soc. Pac., San Francisco, p. 17
 Avni Y., Tananbaum H., 1986, *ApJ*, 305, 83
 Baldwin J., Stone R. P., 1984, *MNRAS*, 206, 241
 Bentz M. C., Katz S., 2015, *PASP*, 127, 67
 Boller T., Brandt W. N., Fink H., 1996, *A&A*, 305, 53
 Boroson T. A., Green R. F., 1992, *ApJS*, 80, 109
 Campitiello S., Celotti A., Ghisellini G., Sbarro T., 2019, *A&A*, 625, A23
 Cann J. M., Satyapal S., Abel N. P., Ricci C., Secrest N. J., Blecha L., Gliozzi M., 2018, *ApJ*, 861, 142
 Cappellari M. et al., 2013, *MNRAS*, 432, 1709
 Cardelli J. A., Clayton G. C., Mathis J. S., 1989, *ApJ*, 345, 245
 Clemens J. C., Crain J. A., Anderson R., 2004, in Moorwood A. F. M., Masanori I., eds, Ground-based Instrumentation for Astronomy. SPIE, Bellingham, p. 331
 Collin-Souffrin S., Dyson J. E., McDowell J. C., Perry J. J., 1988, *MNRAS*, 232, 539
 Contini M., Viegas S. M., 2001, *ApJS*, 132, 211
 Cushing M. C., Vacca W. D., Rayner J. T., 2004, *PASP*, 116, 362
 Dasyra K. M. et al., 2007, *ApJ*, 657, 102
 Elias J. H., Rodgers B., Joyce R. R., Lazo M., Doppmann G., Winge C., Rodríguez-Ardila A., 2006, in Ground-based and Airborne Instrumentation for Astronomy. SPIE, Bellingham, p. 626914
 Fabian A. C. et al., 2013, *MNRAS*, 429, 2917
 Ferguson J. W., Korista K. T., Baldwin J. A., Ferland G. J., 1997, *ApJ*, 487, 122
 Ferland G. J. et al., 2013, *RMxAA*, 49, 137
 Ferland G. J. et al., 2017, *Rev. Mex. Astron. Astrofis.*, 53, 385
 Fernández-Ontiveros J. A., Spinoglio L., Pereira-Santaella M., Malkan M. A., Andreani P., Dasyra K. M., 2016, *ApJS*, 226, 19
 Ferrarese L., Merritt D., 2000, *ApJ*, 539, L9
 Frank J., King A., Raine D. J., 2002, *Accretion Power in Astrophysics*, 3rd edn. Cambridge Univ. Press, Cambridge
 Gardner J. P. et al., 2006, *Space Sci. Rev.*, 123, 485
 Genzel R., Eisenhauer F., Gillessen S., 2010, *Rev. Mod. Phys.*, 82, 3121
 Gravity Collaboration, 2020, *A&A*, 643, A154
 GRAVITY Collaboration, 2021, *A&A*, 648, A117
 Greene J. E., Ho L. C., 2005, *ApJ*, 630, 122
 Gültekin K. et al., 2009, *ApJ*, 698, 198
 Ivezić Ž. et al., 2019, *ApJ*, 873, 111
 Kaspi S., Smith P. S., Netzer H., Maoz D., Jannuzi B. T., Giveon U., 2000, *ApJ*, 533, 631
 Kaspi S., Maoz D., Netzer H., Peterson B. M., Vestergaard M., Jannuzi B. T., 2005, *ApJ*, 629, 61
 Koratkar A. P., Gaskell C. M., 1991, *ApJ*, 370, L61
 Kormendy J., Ho L. C., 2013, *ARA&A*, 51, 511
 Kubota A., Done C., 2018, *MNRAS*, 480, 1247
 Kuraszkiewicz J., Wilkes B. J., Czerny B., Mathur S., 2000, *ApJ*, 542, 692
 Lamperti I. et al., 2017, *MNRAS*, 467, 540
 Landt H., Bentz M. C., Ward M. J., Elvis M., Peterson B. M., Korista K. T., Karovska M., 2008, *ApJS*, 174, 282
 Landt H., Bentz M. C., Peterson B. M., Elvis M., Ward M. J., Korista K. T., Karovska M., 2011, *MNRAS*, 413, L106

- Landt H., Ward M. J., Peterson B. M., Bentz M. C., Elvis M., Korista K. T., Karovska M., 2013, *MNRAS*, 432, 113
- Landt H., Ward M. J., Steenbrugge K. C., Ferland G. J., 2015a, *MNRAS*, 449, 3795
- Landt H., Ward M. J., Steenbrugge K. C., Ferland G. J., 2015b, *MNRAS*, 454, 3688
- Lusso E., Risaliti G., 2017, *A&A*, 602, A79
- Marconi A., Moorwood A. F. M., Salvati M., Oliva E., 1994, *A&A*, 291, 18
- Marziani P. et al., 2019, *A&A*, 627, A88
- Mason R. E. et al., 2015, *ApJS*, 217, 13
- Mazzalay X. et al., 2014, *MNRAS*, 438, 2036
- Molina M., Reines A. E., Latimer C. J., Baldassare V., Salehirad S., 2021, *ApJ*, 922, 155
- Moorwood A. F. M., van der Werf P. P., Kotilainen J. K., Marconi A., Oliva E., 1996, *A&A*, 308, L1
- Moustakas J., Kennicutt Robert C. J., 2006, *ApJS*, 164, 81
- Müller-Sánchez F., Prieto M. A., Hicks E. K. S., Vives-Arias H., Davies R. I., Malkan M., Tacconi L. J., Genzel R., 2011, *ApJ*, 739, 69
- Müller-Sánchez F., Prieto M. A., Mezcuca M., Davies R. I., Malkan M. A., Elitzur M., 2013, *ApJ*, 763, L1
- Nelson C. H., Whittle M., 1996, *ApJ*, 465, 96
- Panda S., 2021, *A&A*, 650, A154
- Panda S., Czerny B., Adhikari T. P., Hryniewicz K., Wildy C., Kuraszkiwicz J., Śniegowska M., 2018, *ApJ*, 866, 115
- Panda S., Marziani P., Czerny B., 2019, *ApJ*, 882, 79
- Park S. et al., 2017, *ApJ*, 847, 125
- Pecaut M. J., Mamajek E. E., 2013, *ApJS*, 208, 9
- Peterson B. M., 1993, *PASP*, 105, 247
- Prieto M. A., Marco O., Gallimore J., 2005, *MNRAS*, 364, L28
- Prieto M. A., Reunanen J., Tristram K. R. W., Neumayer N., Fernandez-Ontiveros J. A., Orienti M., Meisenheimer K., 2010, *MNRAS*, 402, 724
- Reunanen J., Kotilainen J. K., Prieto M. A., 2003, *MNRAS*, 343, 192
- Reynolds C. S., 2019, *Nature Astron.*, 3, 41
- Richards G. T. et al., 2006, *ApJS*, 166, 470
- Riffel R., Rodríguez-Ardila A., Pastoriza M. G., 2006, *A&A*, 457, 61
- Riffel R. A. et al., 2013, *MNRAS*, 429, 2587
- Rodríguez-Ardila A., Viegas S. M., Pastoriza M. G., Prato L., Donzelli C. J., 2002, *ApJ*, 572, 94
- Rodríguez-Ardila A., Contini M., Viegas S. M., 2005, *MNRAS*, 357, 220
- Rodríguez-Ardila A., Prieto M. A., Viegas S., Gruenwald R., 2006, *ApJ*, 653, 1098
- Rodríguez-Ardila A., Prieto M. A., Portilla J. G., Tejeiro J. M., 2011, *ApJ*, 743, 100
- Rodríguez-Ardila A., Prieto M. A., Mazzalay X., Fernández-Ontiveros J. A., Luque R., Müller-Sánchez F., 2017, *MNRAS*, 470, 2845
- Salviander S., Shields G. A., Gebhardt K., Bonning E. W., 2006, *New Astron. Rev.*, 50, 803
- Schlafly E. F., Finkbeiner D. P., 2011, *ApJ*, 737, 103
- Shakura N. I., Sunyaev R. A., 1973, *A&A*, 24, 337
- Shen Y. et al., 2011, *ApJS*, 194, 45
- Skrutskie M. et al., 2006, *AJ*, 131, 1163
- Vacca W. D., Cushing M. C., Rayner J. T., 2003, *PASP*, 115, 389
- Wilkes B. J., Tananbaum H., Worrall D. M., Avni Y., Oey M. S., Flanagan J., 1994, *ApJS*, 92, 53
- Winter L. M., Veilleux S., McKernan B., Kallman T. R., 2012, *ApJ*, 745, 107
- Woo J.-H., Urry C. M., 2002, *ApJ*, 579, 530
- Zamorani G. et al., 1981, *ApJ*, 245, 357

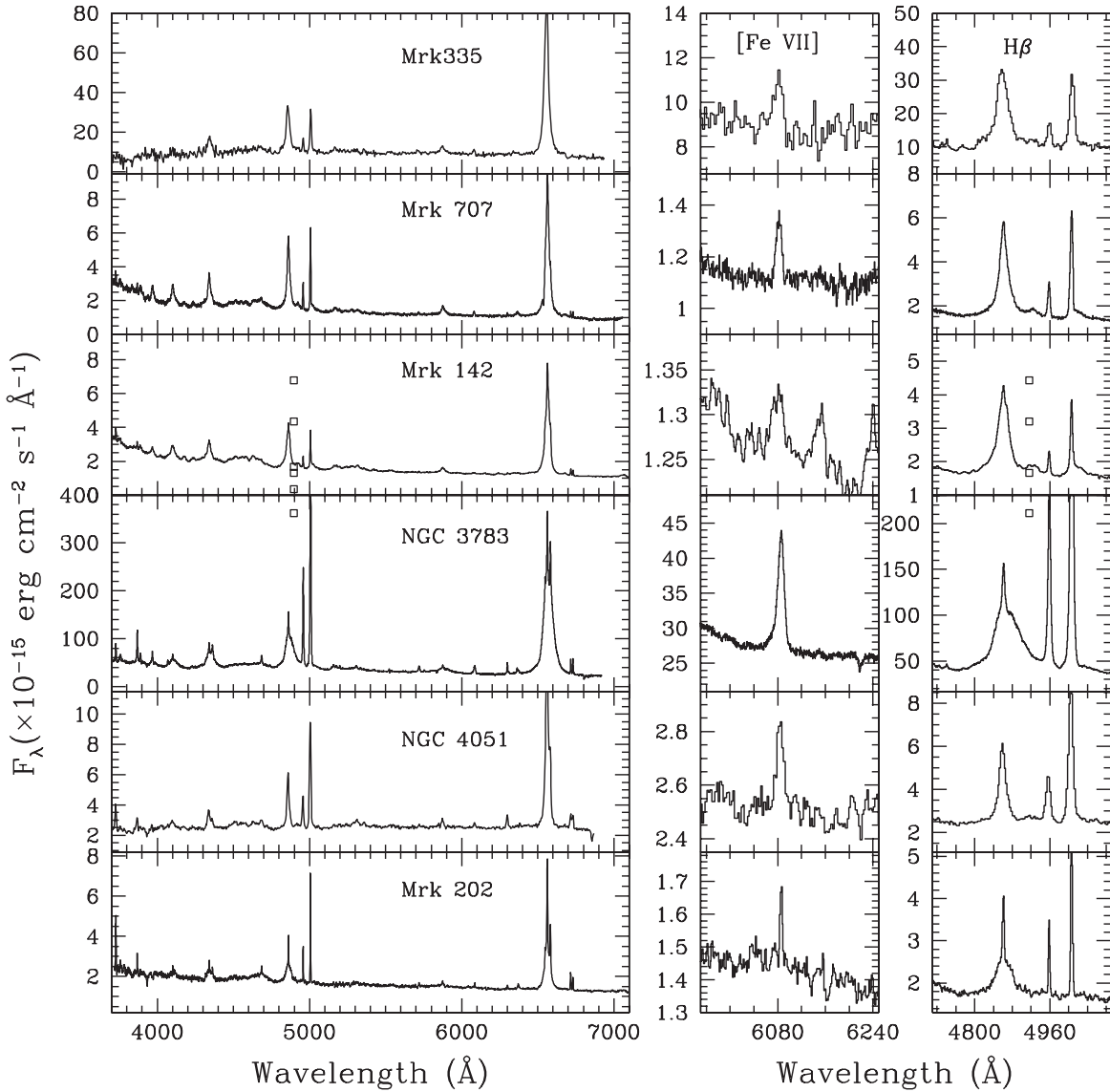
APPENDIX A: OPTICAL SPECTRA

Table A1. Measured broad line H I and coronal line fluxes, in units of 10^{-15} erg cm^{-2} s^{-1} , for the galaxy sample.

Galaxy	H β $\lambda 4861$	Pa β $\lambda 12818$	Br γ $\lambda 21657$	[Fe VII] $\lambda 6087$	[S VIII] $\lambda 9913$	[Si X] $\lambda 14203$	[Si VI] $\lambda 19630$
Mrk 335	712.68 \pm 44.13	170 \pm 5	26.7 \pm 3.1	55.12 \pm 5.50	3.76 \pm 1.00	7.45 \pm 2.00	10.6 \pm 2.0
Fairall 9	490.25 \pm 30.12	107.95 \pm 8.40	43.1 \pm 4.7	18.4 \pm 1.33	4.23 \pm 0.52	8.16 \pm 0.67	4.00 \pm 0.52
NGC 863	...	49 \pm 3	10.40 \pm 2.94	2.54 \pm 0.14
3C 120	...	222.9 \pm 5.94	46.34 \pm 6.55	...	2.97 \pm 0.17	9.96 \pm 2.47	15.48 \pm 1.96
Mrk 707	107.67 \pm 3.31	...	4.76 \pm 0.39	2.60 \pm 0.23	1.4 \pm 0.27	3.18 \pm 0.31	1.82 \pm 0.09
Mrk 110	52.22 \pm 1.43	2.43 \pm 0.08
NGC 3227	...	168.74 \pm 10.23	20.0 \pm 3.92	...	1.97 \pm 0.6	...	14.9 \pm 2.6
Mrk 142	86.05 \pm 0.70	1.67 \pm 0.35
SBS 1116+583A	47.23 \pm 1.93	0.46 \pm 0.08
PG 1126-041	...	101.83 \pm 3.7	13.3 \pm 0.73	...	2.58 \pm 0.21	4.32 \pm 0.45	3.71 \pm 0.17
NGC 3783	4693.0 \pm 157.0	348.70 \pm 19.06	60.40 \pm 9.82	242.0 \pm 6.48	8.12 \pm 0.86	17.51 \pm 2.67	25.6 \pm 3.71
Mrk 1310	34.9 \pm 0.72	11.4 \pm 1.1	1.4 \pm 0.4	1.10 \pm 0.05	0.79 \pm 0.10	0.83 \pm 0.19	0.74 \pm 0.11
NGC 4051	48.22 \pm 2.44	66.6 \pm 1.7	13.1 \pm 0.8	5.95 \pm 0.51	13.7 \pm 2.0	22.2 \pm 1.1	12.5 \pm 1.2
NGC 4151	7585 \pm 79	712.48 \pm 8.77	125.0 \pm 10.81	151.0 \pm 3.47	40.5 \pm 2.1	37.7 \pm 1.6	64.0 \pm 1.3
Mrk 202	41.9 \pm 2.14	1.41 \pm 0.15
Mrk 766	829 \pm 30	117.8 \pm 1.8	20.0 \pm 2.26	24.0 \pm 1.20	5.3 \pm 0.2	6.3 \pm 0.4	15.6 \pm 0.9
Mrk 50	160 \pm 5.0	0.77 \pm 0.15
NGC 4395	11.0 \pm 0.2	30.5 \pm 1.1	1.9 \pm 0.2	1.03 \pm 0.06	1.6 \pm 0.2	0.57 \pm 0.09	2.2 \pm 0.1
Mrk 771	125.25 \pm 2.44	3.88 \pm 0.23
NGC 4748	...	60.1 \pm 2.2	9.7 \pm 0.5	...	8.2 \pm 2.5	3.4 \pm 1.1	9.0 \pm 0.3
PG 1307+085	172.0 \pm 2.4	1.65 \pm 0.28
MGC-6-30-15	1100.0 \pm 4.0	18.8 \pm 2.15

Table A1 – *continued*

Galaxy	H β $\lambda 4861$	Pa β $\lambda 12818$	Br γ $\lambda 21657$	[Fe VII] $\lambda 6087$	[S VIII] $\lambda 9913$	[Si X] $\lambda 14203$	[Si VI] $\lambda 19630$
NGC 5548	314.0 ± 9.77	49.3 ± 2.9	16.3 ± 2.0	13.9 ± 0.65	6.0 ± 0.4	5.6 ± 0.4	10.0 ± 0.9
PG1448+273	2.40 ± 0.10	...	0.66 ± 0.06	...	1.6 ± 0.2
Mrk 290	239.0 ± 5.25	5.44 ± 0.36
Mrk 841	435.56 ± 12.0	146.7 ± 10.4	26.1 ± 7.5	3.42 ± 0.94	3.5 ± 0.2	2.2 ± 0.5	5.2 ± 0.1
3C 390.3	433.12 ± 7.1	7.82 ± 0.39
NGC 6814	...	81.0 ± 13.3	11.9 ± 3.5	...	0.55 ± 0.23	...	2.00 ± 0.29
Mrk 509	...	1824.7 ± 77.9	349.0 ± 21.8	58.8 ± 5.1
Ark 564	160.1 ± 2.2	59.0 ± 1.5	5.7 ± 0.4	9.0 ± 1.14	5.9 ± 0.4	17.9 ± 0.3	6.2 ± 0.3
NGC 7469	854.59 ± 12.0	153.1 ± 7.3	20.7 ± 1.4	17.9 ± 0.96	5.6 ± 0.8	11.4 ± 1.3	12.4 ± 0.5

**Figure A1.** Optical Spectra of the AGN sample in rest wavelength. For each galaxy, the left-hand panel shows the full spectrum. The two smaller panels to the left shows [Fe VII] $\lambda 6087$ and the H β line.

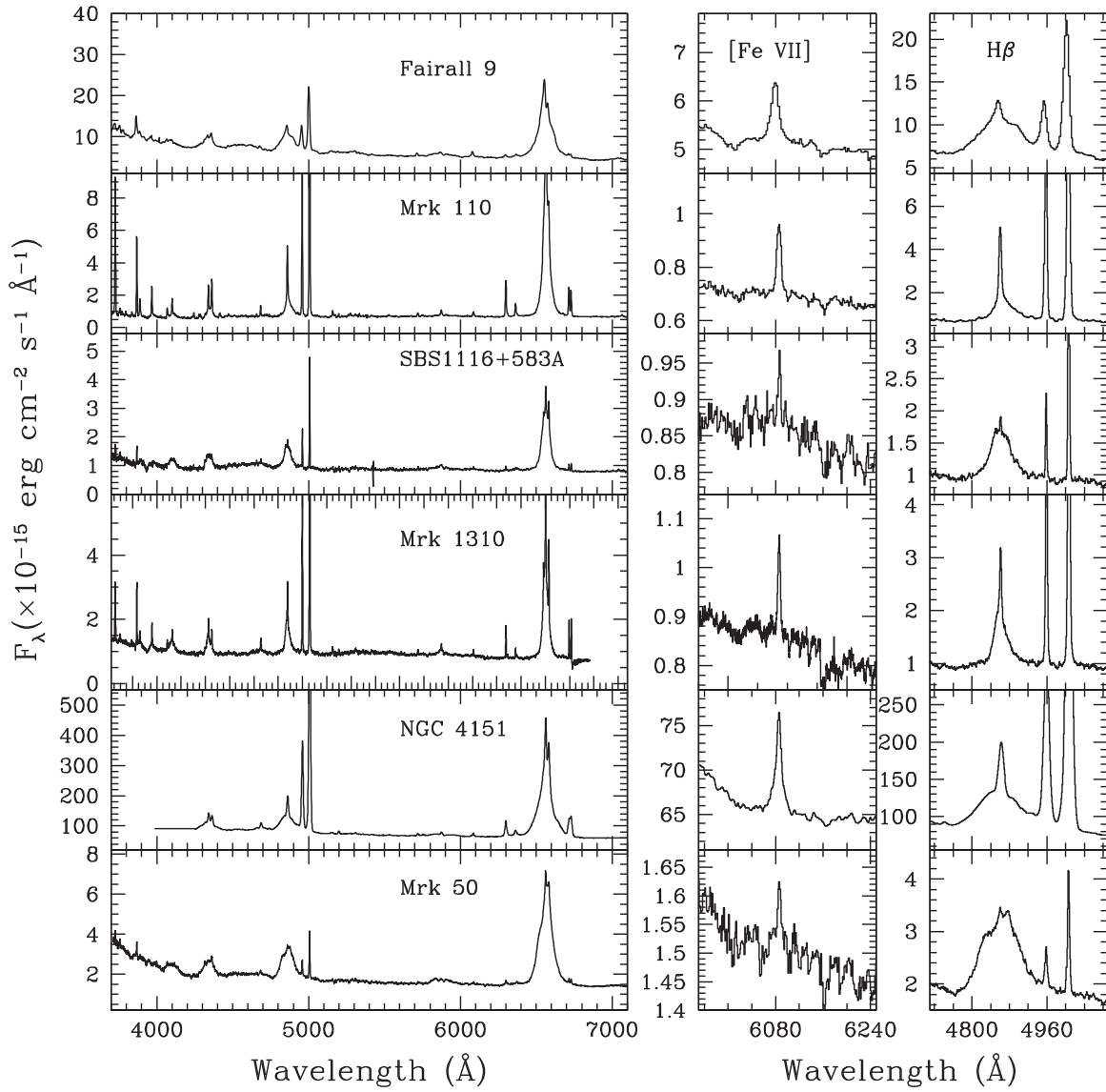


Figure A2. Cont. Fig. A1.

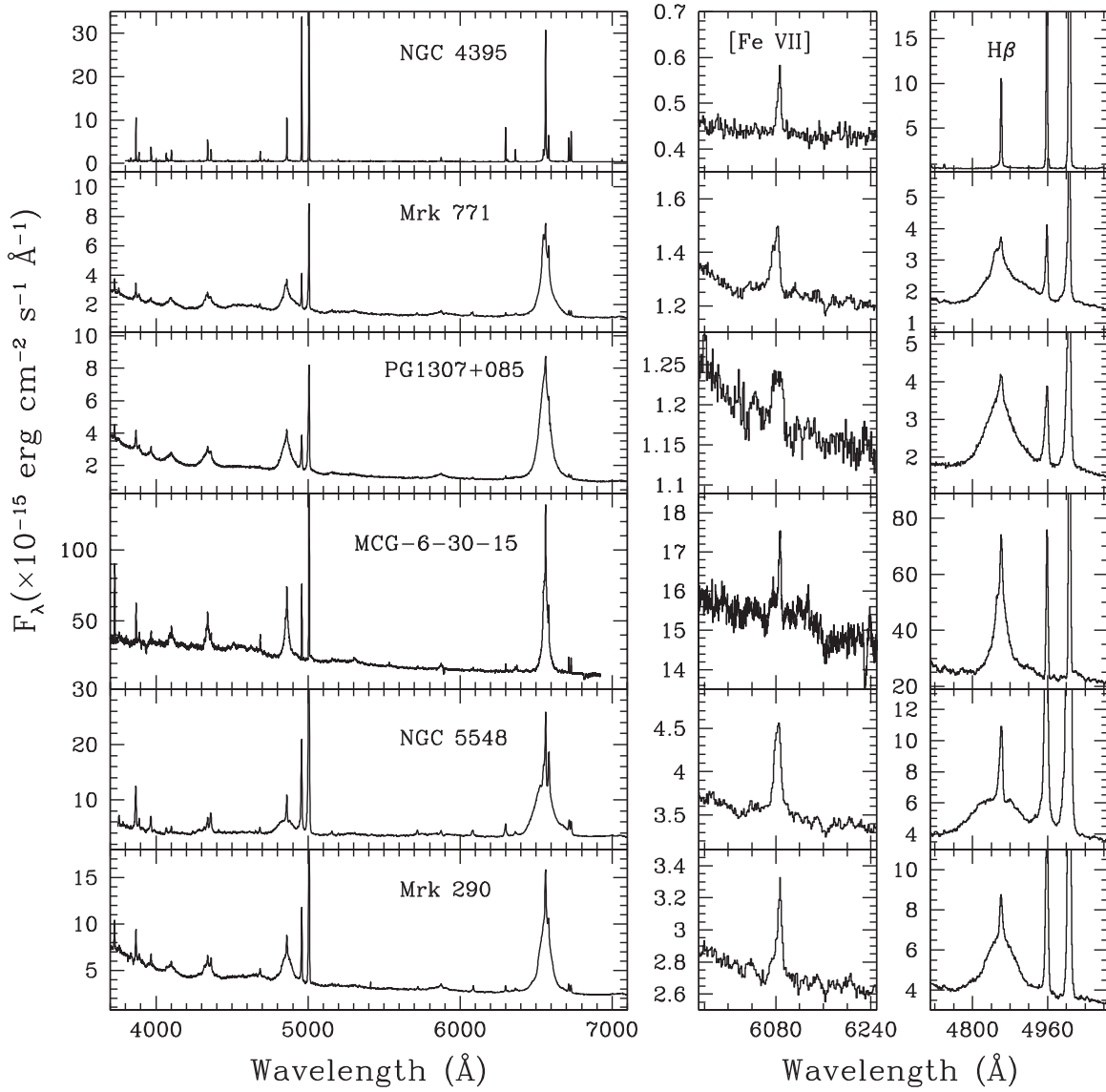


Figure A3. Cont. Fig. A1.

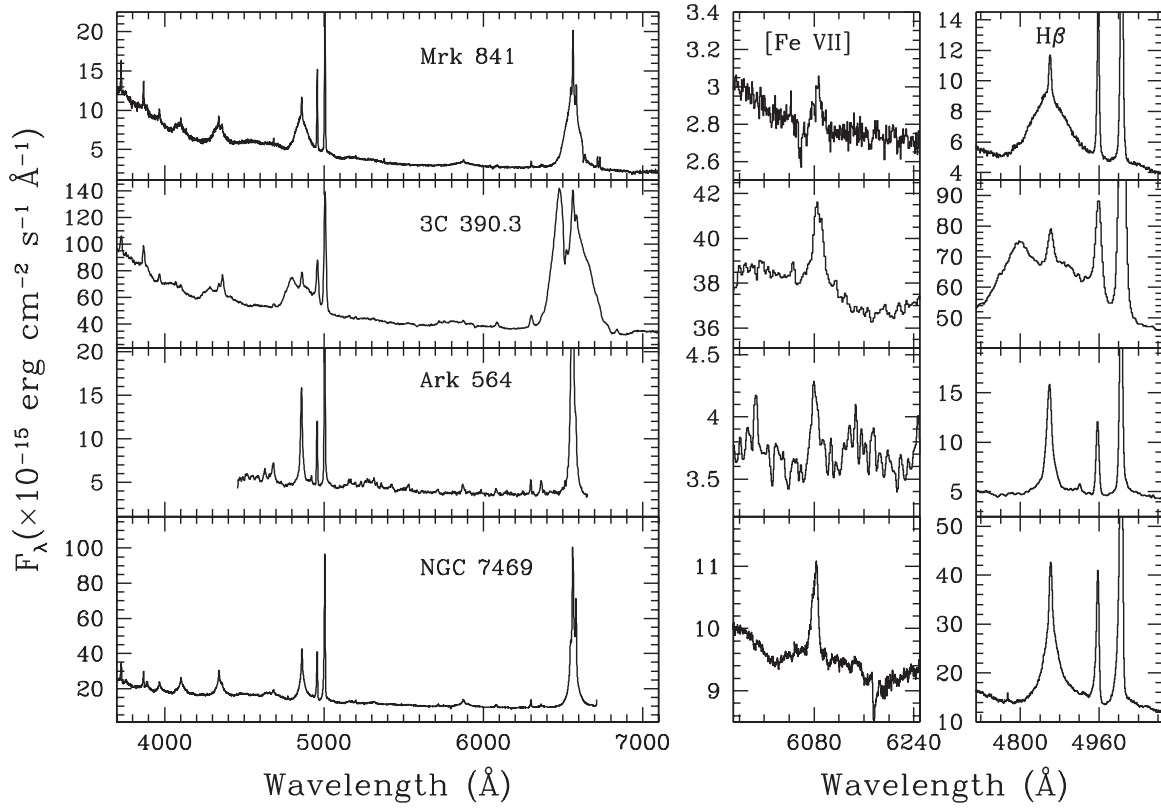


Figure A4. Cont. Fig. A1.

Downloaded from https://academic.oup.com/mnras/article/510/1/1010/6442249 by guest on 23 April 2024

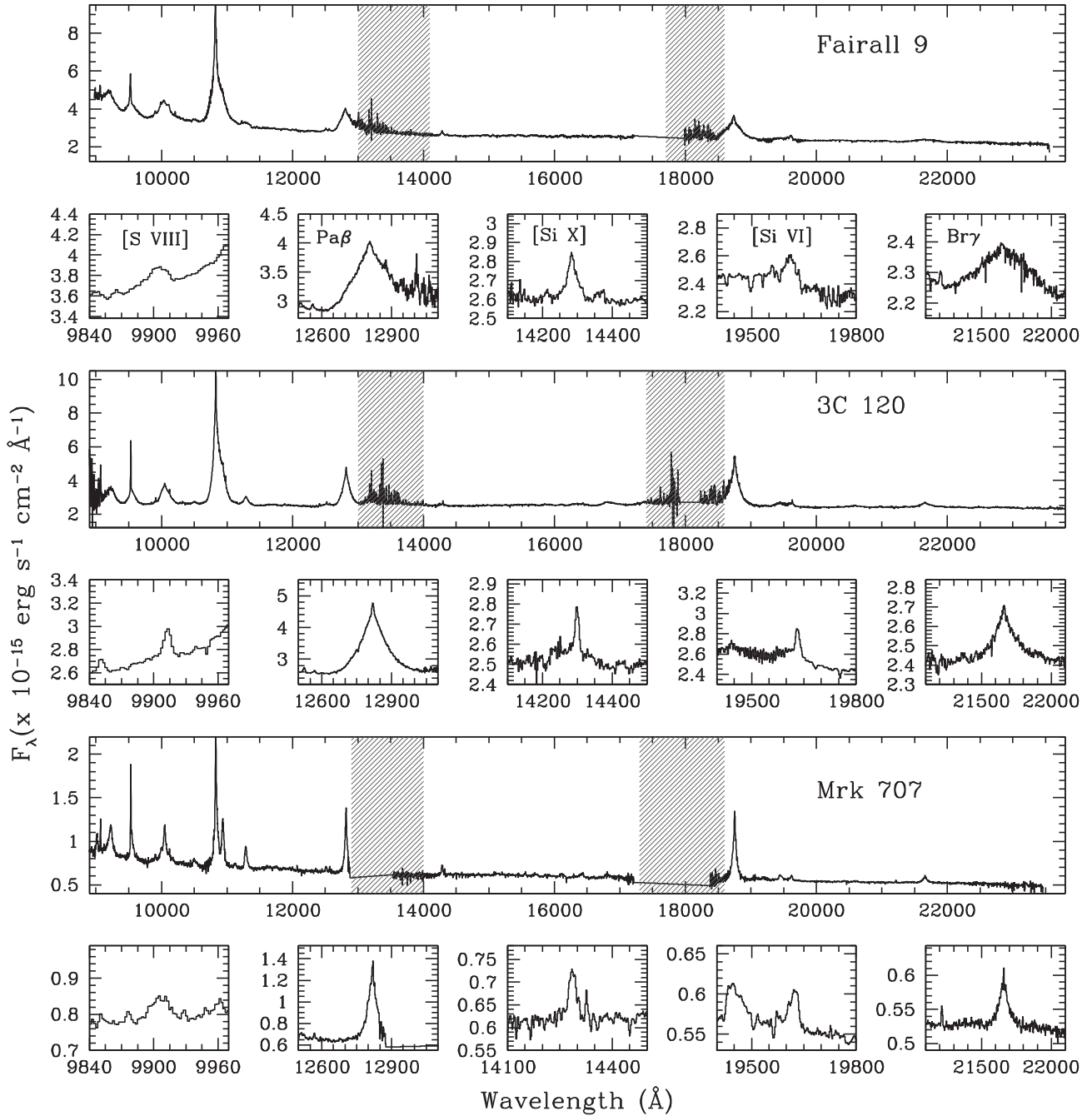


Figure A5. NIR spectra of Fairall 9 (top panels), 3C 120 (middle panels), and Mrk 707 (bottom panels) in rest wavelength. For each AGN, the larger panel displays the observed spectrum in the 9000–23000 Å range. The smaller panels in the following row show a zoom around the most relevant lines to this work. The shaded areas mark regions of bad atmospheric transmission.

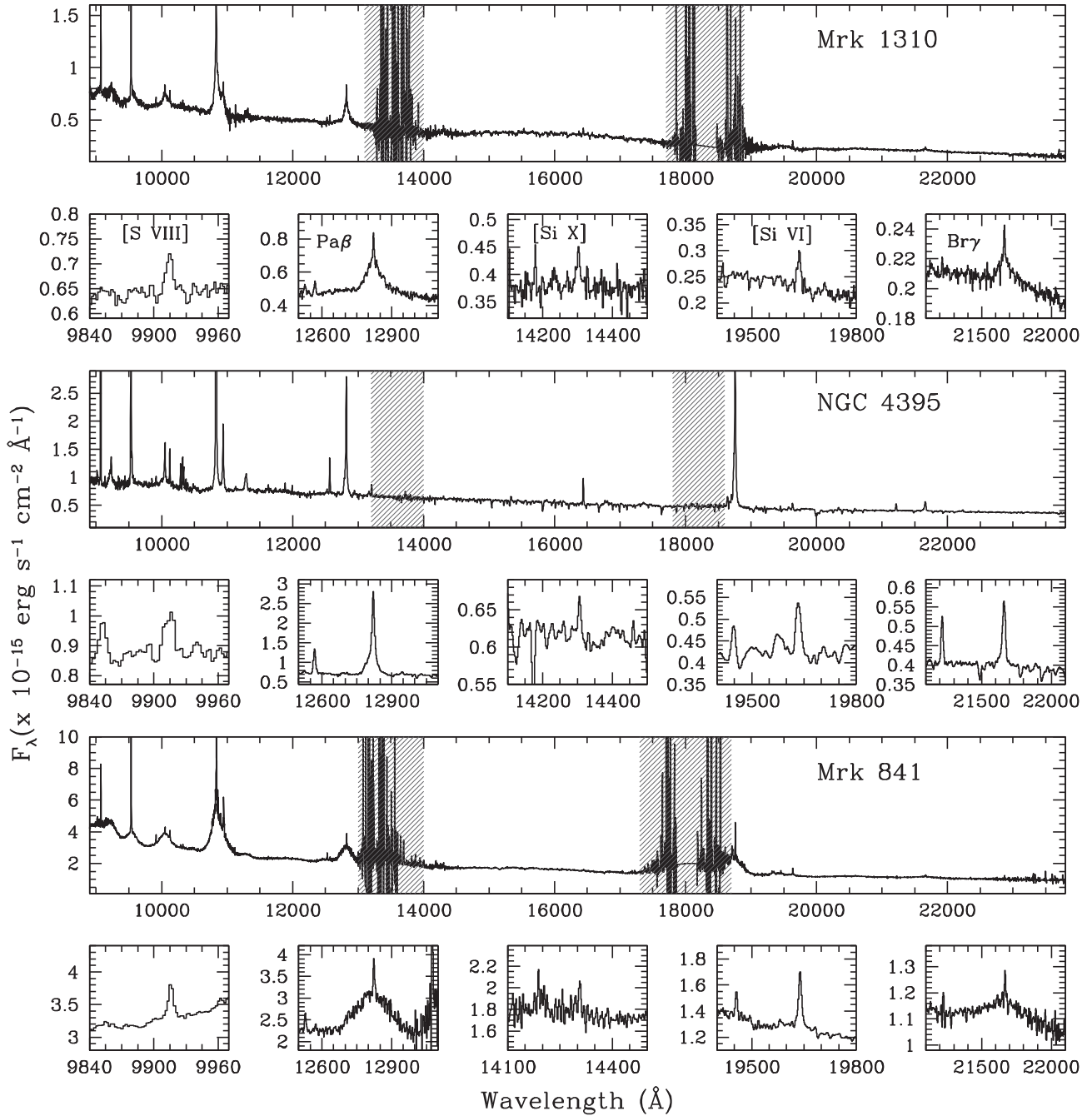


Figure A6. Same as Fig. A5 for Mrk 1310 (top panels), NGC 4395 (middle panels), and Mrk 841 (bottom panels).

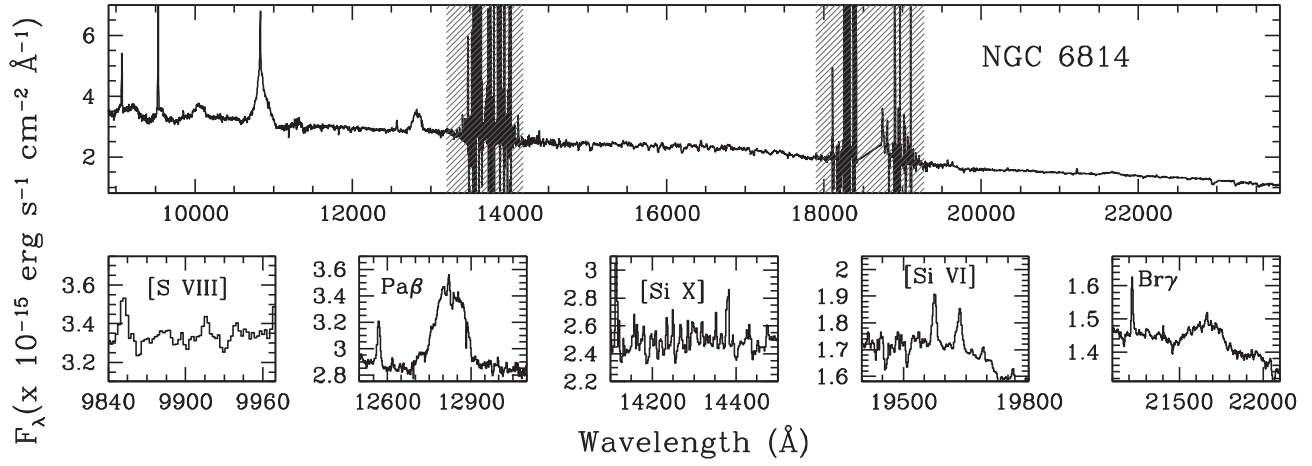


Figure A7. Same as Fig. A5 for NGC 6814.

This paper has been typeset from a $\text{\TeX}/\text{\LaTeX}$ file prepared by the author.